

# Self-consistent Continuum Random Phase Approximation calculations with finite-range interactions

V. De Donno, G. Co'

*Dipartimento di Fisica, Università del Salento and,  
INFN Sezione di Lecce, Via Arnesano, I-73100 Lecce, ITALY*

M. Anguiano, A. M. Lallena

*Departamento de Física Atómica, Molecular y Nuclear,  
Universidad de Granada, E-18071 Granada, SPAIN*

(Dated: November 5, 2018)

We present a technique which treats, without approximations, the continuum part of the excitation spectrum in Random Phase Approximation calculations with finite-range interactions. The interaction used in the Hartree-Fock calculations to generate the single particle basis is also used in the Continuum Random Phase Approximation calculations. We show results for the electric dipole and quadrupole excitations in the  $^{16}\text{O}$ ,  $^{22}\text{O}$ ,  $^{24}\text{O}$ ,  $^{40}\text{Ca}$ ,  $^{48}\text{Ca}$  and  $^{52}\text{Ca}$  nuclei. We compare our results with those of the traditional discrete Random Phase Approximation, with the continuum independent particle model results and with those obtained by a phenomenological Random Phase Approximation approach. We study the relevance of the continuum, of the residual interaction and of the self-consistency. We also compare our results with the available total photoabsorption cross section data.

PACS numbers: 21.60.Jz, 24.30.Cz, 25.20.Dc

## I. INTRODUCTION

In the next few years, radioactive ion beams facilities will provide a large amount of data on unstable nuclei. The description of the structure of these nuclei is a challenge for the nuclear many-body theories which have been mainly tested on stable nuclei.

The starting point of our description of nuclear systems is the many-body Schrödinger equation with a two-body potential built to describe elastic nucleon-nucleon (NN) cross sections and deuteron properties [1, 2]. To this two-body potential we add a three-body force whose parameters are chosen to reproduce the  $^3\text{H}$  binding energy [3, 4]. Modern microscopic calculations, which solve the many-body Schrödinger equation without approximations, describe well the structure of nuclear few-body systems as well as that of light nuclei [5, 6]. These results establish the validity of the non relativistic description of atomic nuclei. Unfortunately, the computational complexity of these microscopic calculations hinders their application to medium and heavy nuclei.

In recent years, there have been great advances in theories which solve the many-body Schrödinger equation with microscopic interactions by doing well controlled approximations [7–12]. The results are very promising but the calculations are still computationally rather involved. Probably, the development of these approaches will not be rapid enough to cover the requirements for the description of the data which will appear in the near future. We think that, for this purpose, effective theories will play a fundamental role.

Effective theories search for solutions of the many-body Schrödinger equation in a subspace of the full Hilbert space. Usually this subspace is chosen to be formed by Slater determinants. This restriction requires the modification of the NN interaction in order to reproduce the energy eigenvalues of the microscopic theory. By using Feshbach's projection techniques, it is possible to obtain a formal expression which relates microscopic and effective interactions [13]. In the common practice, the effective interaction is parametrized, and the values of the parameters are chosen to reproduce some experimental data.

For example, in the Jülich approach [14, 15], which we shall call here phenomenological Random Phase Approximation (RPA) approach, the single particle (s.p.) wave functions are produced by a Woods-Saxon potential whose parameters are chosen to reproduce at best charge radii and s.p. energies near the Fermi level of the nucleus under investigation. The values of the interaction parameters are selected to reproduce the excitation energy of some particularly collective state, for example, in the  $^{208}\text{Pb}$  nucleus, that of the low-lying  $3^-$  state. The phenomenological approach has been applied in the '80s of the past century to describe, and predict, with success the excitation of the low-lying spectrum and of the giant resonances mainly in doubly-magic nuclei. This phenomenological approach, based on the Landau-Migdal theory of finite Fermi systems [16], requires the knowledge of a quite a number of observables in order

to select the RPA input parameters, i.e. the s.p. basis and the effective interaction. The philosophy of the approach requires to change the input for every nucleus considered, therefore, despite of its success, the phenomenological RPA approach is not suitable to predict the structure of experimentally unknown nuclei.

For this purpose, self-consistent RPA approaches are more useful. In these approaches, s.p. wave functions and energies are obtained by solving the Hartree-Fock (HF) equations. Since the effective interaction used in HF is also used in the RPA calculation this type of calculations is called self-consistent. In the self-consistent approaches the values of the parameters of the effective interaction are chosen to reproduce binding energies, and charge radii, of a large number of nuclei. This fit produces an effective interaction to be used in all the regions of the nuclear chart, including those so far unexplored by the experiment.

Self-consistent RPA approaches have greater prediction power than phenomenological approaches, but they require higher level of accuracy and stability of the calculations. For example, the dimension of the s.p. configuration space, beyond a certain size, is not a problem in the phenomenological approach since the effects of the truncation of the s.p. basis are taken into account by changing the values of the interaction parameters. This procedure cannot be used any more in self-consistent approaches, since the interaction parameters are chosen once forever in HF calculations. This drawback of the self-consistent RPA approach is avoided if the full s.p. configuration space is used in the calculation. This implies a proper treatment of the continuum part of the s.p. spectrum.

Self-consistent RPA approaches which consider the continuum have been proposed already in the second half of the '70s [17–23], but they are applicable only if zero-range interactions are used. In this case the continuum RPA (CRPA) equations simplify, since direct and exchange matrix elements assume the same expressions, i. e. they are proportional.

Zero-range effective interactions have the great merit of simplifying the calculations. There are however various drawbacks in their use, many of them discussed already in Ref. [24] where the D1 parameterization of the finite-range Gogny interaction was proposed. Here we would like to mention some other aspects more directly related to the present work. In RPA calculations zero-range interactions produce more collectivity than finite-range interactions. The difference becomes larger with the increasing value of the momentum transfer [25]. In addition, finite-range interactions provide a better description of unnatural parity excitations [15, 26, 27]. Finally, finite-range interactions are more directly comparable with microscopic NN force.

The reasons presented above motivated our work. We developed a formalism capable to solve the CRPA equations with finite-range interactions. The main problem we had to face was the treatment of the exchange terms of the interaction matrix elements. In the literature there are few examples of CRPA calculations done with finite-range interactions [28, 29], and, to the best of our knowledge, only a single case of self-consistent CRPA calculation [30]. The relativistic self-consistent calculations of Ref. [31] use finite range interactions, but in the so-called Hartree approximation where the exchange terms are neglected. Our approach, which will be described in Sect. II, follows the lines of that proposed by the Jülich group at the beginning of the '90s [29]. There are, however, important differences due to the different manner of generating the s.p. bases. In the Jülich case they are produced by using a Woods-Saxon potential while in our approach with a HF calculation.

Details and basic ingredients of the calculations, such as interactions, expansion basis, test of convergence etc., are presented in Sect. III. A discussion of a selected set of results is done in Sect. IV. We have calculated charge conserving excitations in three oxygen isotopes and in three calcium isotopes. We compare our CRPA results with those obtained from discrete RPA calculations, with the results of the phenomenological RPA approach and also with results obtained by switching off the residual interaction in the RPA calculations. Following the notation of Ref. [32] we shall label independent particle model (IPM) the results of this last type of calculations. In Sect. V we summarize the main results of our work and we draw our conclusions.

## II. FORMALISM

The RPA theory describes the excited state of a many-body system as linear combination of particle-hole (*ph*), and hole-particle (*hp*) excitations. This implies the existence of a s.p. basis which, in our calculations, is generated by solving the HF equations:

$$\mathcal{H} [\phi_k(\mathbf{r})] = -\frac{\hbar^2}{2m} \nabla^2 \phi_k(\mathbf{r}) + \mathcal{U}(\mathbf{r}) \phi_k(\mathbf{r}) - \int d^3 r' \mathcal{W}(\mathbf{r}, \mathbf{r}') \phi_k(\mathbf{r}') = \epsilon_k \phi_k(\mathbf{r}), \quad (1)$$

where we have indicated with  $\mathcal{H}$  and  $\phi_k$  the s.p. hamiltonian and wave function respectively, with  $\mathcal{U}$  the Hartree potential

$$\mathcal{U}(\mathbf{r}) = \sum_{\alpha=1}^8 \sum_{j \leq F} \int d^3 r' \phi_j^*(\mathbf{r}') V_{\alpha}(\mathbf{r}, \mathbf{r}') \phi_j(\mathbf{r}'), \quad (2)$$

with  $\mathcal{W}$  the Fock-Dirac potential

$$\mathcal{W}(\mathbf{r}, \mathbf{r}') = \sum_{\alpha=1}^8 \sum_{j \leq F} \phi_j^*(\mathbf{r}') V_{\alpha}(\mathbf{r}, \mathbf{r}') \phi_j(\mathbf{r}), \quad (3)$$

and with  $\epsilon_k$  the energy eigenvalue of the  $k$ -th s.p. state. In the above expressions, the sums on the s.p. states are restricted to those with energy lower than the Fermi energy, i.e. to the hole states.

In our calculations we consider a two-body NN interaction of the form

$$V_{\alpha}(\mathbf{r}_i, \mathbf{r}_j) = v_{\alpha}(|\mathbf{r}_i - \mathbf{r}_j|) O_{i,j}^{\alpha}, \quad \text{with } \alpha = 1, 2, \dots, 8, \quad (4)$$

where  $v_{\alpha}$  are scalar functions of the distance between the two interacting nucleons, and  $O^{\alpha}$  indicates the type of operator dependence

$$O_{i,j}^{\alpha} : 1, \boldsymbol{\tau}(i) \cdot \boldsymbol{\tau}(j), \boldsymbol{\sigma}(i) \cdot \boldsymbol{\sigma}(j), \boldsymbol{\sigma}(i) \cdot \boldsymbol{\sigma}(j) \boldsymbol{\tau}(i) \cdot \boldsymbol{\tau}(j), \\ S(i, j), S(i, j) \boldsymbol{\tau}(i) \cdot \boldsymbol{\tau}(j), \mathbf{l}_{ij} \cdot \mathbf{s}_{ij}, \mathbf{l}_{ij} \cdot \mathbf{s}_{ij} \boldsymbol{\tau}(i) \cdot \boldsymbol{\tau}(j). \quad (5)$$

In the above expression we have indicated with  $\boldsymbol{\sigma}$  the Pauli matrix operator acting on the spin variable, with  $\boldsymbol{\tau}$  the analogous operator for the isospin, and with

$$S(i, j) = 3 \frac{[\boldsymbol{\sigma}(i) \cdot (\mathbf{r}_i - \mathbf{r}_j)] [\boldsymbol{\sigma}(j) \cdot (\mathbf{r}_i - \mathbf{r}_j)]}{(\mathbf{r}_i - \mathbf{r}_j)^2} - \boldsymbol{\sigma}(i) \cdot \boldsymbol{\sigma}(j) \quad (6)$$

the usual tensor operator. The terms  $\alpha = 7, 8$  indicate the spin-orbit contributions of the force. We include these last terms only in the HF calculations and we consider them in a zero-range approximation as it is done in Ref. [24].

We solve the HF equations in a spherical basis, and we express the s.p. wave functions as

$$\phi_k^t(\mathbf{r}) = \phi_{nljm}^t(\mathbf{r}) = R_{nlj}^t(r) \sum_{s\mu} \langle l\mu \frac{1}{2}s | jm \rangle Y_{l\mu}(\Omega) \chi_s. \quad (7)$$

In the above equation, we have indicated with  $n, l, j$  and  $m$  the principal quantum number, the orbital angular momentum, the total angular momentum and its  $z$ -axis projection, respectively. We use  $r$  to indicate the distance from the center of the nucleus, and  $\Omega$  to indicate the usual angular coordinates of the polar spherical system. The symbol  $\langle | \rangle$  indicates the Clebsch-Gordan coefficient,  $Y_{l\mu}$  is the spherical harmonics and  $\chi_s$  the Pauli spinor for the spin. We call  $t$  the third component of the isospin and we use the convention  $t = 1/2$  for protons and  $t = -1/2$  for neutrons. The radial part of the s.p. wave function satisfies the closure relation

$$\sum_{\epsilon_i < \epsilon_F} \delta_{ik} R_i(r) R_i^*(r') + \oint_{\epsilon_k} R_k(r, \epsilon_k) R_k^*(r', \epsilon_k) = \delta(r - r'), \quad (8)$$

where we have introduced the symbol

$$\oint_{\epsilon_k} \equiv \sum_{\epsilon_F \leq \epsilon_k \leq 0} + \int_0^{\infty} d\epsilon_k \quad (9)$$

to indicate a sum and an integration on all the s.p. energies above the Fermi surface. In the following, we shall indicate explicitly the dependence on the s.p. energies  $\epsilon_k$  which can assume both discrete and continuum values. We shall use the index  $h$  to indicate all the quantum numbers identifying a hole s.p. state, energy included, while the symbol  $p$  will indicate all the quantum numbers of the particle state, but the s.p. energy  $\epsilon_p$ .

A nuclear excited state  $|\nu\rangle \equiv |J, \Pi, \omega\rangle$  is characterized by its total angular momentum  $J$ , parity  $\Pi$  and excitation energy  $\omega$ . In the CRPA theory, the expression of the operator that applied to the ground state generates the excited state  $|\nu\rangle$  can be expressed as

$$Q_{\nu}^{\dagger} = \sum_{ph} \oint_{\epsilon_p} \left[ X_{ph}^{\nu}(\epsilon_p) a_p^{\dagger}(\epsilon_p) a_h - Y_{ph}^{\nu}(\epsilon_p) a_h^{\dagger} a_p(\epsilon_p) \right], \quad (10)$$

where we have indicated with  $a^\dagger$  and  $a$  the usual particle creation and annihilation operators and with  $X$  and  $Y$  the RPA amplitudes. The CRPA secular equations whose solution provides the values of  $X$  and  $Y$  can be written as

$$(\epsilon_p - \epsilon_h - \omega) X_{ph}^\nu(\epsilon_p) + \sum_{p'h'} \oint_{\epsilon_{p'}} [v_{ph,p'h'}^J(\epsilon_p, \epsilon_{p'}) X_{p'h'}^\nu(\epsilon_{p'}) + u_{ph,p'h'}^J(\epsilon_p, \epsilon_{p'}) Y_{p'h'}^\nu(\epsilon_{p'})] = 0, \quad (11)$$

$$(\epsilon_p - \epsilon_h + \omega) Y_{ph}^\nu(\epsilon_p) + \sum_{p'h'} \oint_{\epsilon_{p'}} [v_{ph,p'h'}^{J*}(\epsilon_p, \epsilon_{p'}) Y_{p'h'}^\nu(\epsilon_p) + u_{ph,p'h'}^{J*}(\epsilon_p, \epsilon_{p'}) X_{p'h'}^\nu(\epsilon_{p'})] = 0. \quad (12)$$

In the above equations, the interaction terms have been defined as

$$v_{ph,p'h'}^J(\epsilon_p, \epsilon_{p'}) = v_{ph,p'h'}^{J,\text{dir}}(\epsilon_p, \epsilon_{p'}) - v_{ph,p'h'}^{J,\text{exc}}(\epsilon_p, \epsilon_{p'}), \quad (13)$$

and

$$u_{ph,p'h'}^J(\epsilon_p, \epsilon_{p'}) = (-1)^{j_{p'}+j_{h'}-J} v_{ph,h'p'}^J(\epsilon_p, \epsilon_{p'}), \quad (14)$$

with

$$v_{ph,p'h'}^{J,\text{dir}}(\epsilon_p, \epsilon_{p'}) = \int dr_1 r_1^2 \int dr_2 r_2^2 R_p^*(r_1, \epsilon_p) R_{h'}^*(r_2) V_{ph,p'h'}^{J,\text{dir}}(r_1, r_2) R_h(r_1) R_{p'}(r_2, \epsilon_{p'}), \quad (15)$$

$$v_{ph,p'h'}^{J,\text{exc}}(\epsilon_p, \epsilon_{p'}) = \int dr_1 r_1^2 \int dr_2 r_2^2 R_p^*(r_1, \epsilon_p) R_{h'}^*(r_2) V_{ph,p'h'}^{J,\text{exc}}(r_1, r_2) R_{p'}(r_1, \epsilon_{p'}) R_h(r_2). \quad (16)$$

In an analogous way, according to Eq. (14), we define the corresponding  $u$  functions. We have used the following definitions for the quantities related to the interaction

$$V_{ph,p'h'}^{J,\text{dir}}(r_1, r_2) = \sum_{\alpha=1}^6 V_\alpha(r_1, r_2) \mathcal{A}_{ph,p'h'}^{J,\alpha,\text{dir}}, \quad (17)$$

$$V_{ph,p'h'}^{J,\text{exc}}(r_1, r_2) = \sum_{\alpha=1}^6 V_\alpha(r_1, r_2) \mathcal{A}_{ph,p'h'}^{J,\alpha,\text{exc}}, \quad (18)$$

$$\mathcal{A}_{ph,p'h'}^{J,\alpha,\text{dir}} = \sum_K (-1)^{j_h+j_{p'}+K} \hat{K} \left\{ \begin{matrix} j_p & j_h & J \\ j_{p'} & j_{h'} & K \end{matrix} \right\} \langle j_p j_{h'} K \| V_\alpha(\Omega) \| j_h j_{p'} K \rangle, \quad (19)$$

$$\mathcal{A}_{ph,p'h'}^{J,\alpha,\text{exc}} = \sum_K \hat{K} \left\{ \begin{matrix} j_p & j_h & J \\ j_{p'} & j_{h'} & K \end{matrix} \right\} \langle j_p j_{h'} K \| V_\alpha(\Omega) \| j_{p'} j_h K \rangle. \quad (20)$$

Here for the angular momentum quantum numbers we used the notation  $\hat{a} = \sqrt{2a+1}$ . The terms in curly brackets are the Racah  $6j$  symbol and the double bars indicate the reduced matrix element as defined by the Wigner-Eckart theorem. In our work we adopt the phase conventions of Ref. [33].

In the above equations we have factorized the two-body NN interaction (4) in a radial part  $V_\alpha(r_1, r_2)$ , depending only on the moduli of the positions of the two-interacting nucleons, and in an angular and operator dependent part  $V_\alpha(\Omega)$ . We have done this factorization by using the Fourier transformed expression of the NN interaction.

Our method of solving the CRPA equations consists in reformulating the secular equations (11) and (12) with new unknown functions which do not have an explicit dependence on the continuous particle energy  $\epsilon_p$ . This is the same approach adopted in Refs. [28, 29], but in our case the s.p. wave functions are generated by a HF calculation. For this reason, we present here, with some detail, the various steps bringing to the new CRPA secular equations. The new unknowns are the channel functions  $f$  and  $g$  defined as:

$$f_{ph}^\nu(r) = \oint_{\epsilon_p} X_{ph}^\nu(\epsilon_p) R_p(r, \epsilon_p), \quad (21)$$

and

$$g_{ph}^\nu(r) = \oint_{\epsilon_p} Y_{ph}^{\nu*}(\epsilon_p) R_p(r, \epsilon_p). \quad (22)$$

The first step of this procedure consists in multiplying Eqs. (11) and (12) by  $R_p(r, \epsilon_p)$ , the radial part of the particle wave function. Considering Eq. (1), we obtain for the left hand side of Eq. (11)

$$(\epsilon_p - \epsilon_h - \omega) R_p(r, \epsilon_p) X_{ph}^\nu(\epsilon_p) = \mathcal{H} [R_p(r, \epsilon_p) X_{ph}^\nu(\epsilon_p)] - (\epsilon_h + \omega) R_p(r, \epsilon_p) X_{ph}^\nu(\epsilon_p). \quad (23)$$

The second step of the procedure is to integrate on  $\epsilon_p$ , the particle energy. For the first term in the right hand side of the above equation we obtain, using again Eq. (1),

$$\begin{aligned} \oint_{\epsilon_p} \mathcal{H} [R_p(r, \epsilon_p) X_{ph}^\nu(\epsilon_p)] &= -\frac{\hbar^2}{2m} \nabla^2 \oint_{\epsilon_p} R_p(r, \epsilon_p) X_{ph}^\nu(\epsilon_p) + \mathcal{U}(\mathbf{r}) \oint_{\epsilon_p} R_p(r, \epsilon_p) X_{ph}^\nu(\epsilon_p) \\ &\quad - \int d^3 r' \mathcal{W}(\mathbf{r}, \mathbf{r}') \oint_{\epsilon_p} R_p(r, \epsilon_p) X_{ph}^\nu(\epsilon_p) \\ &= -\frac{\hbar^2}{2m} \nabla^2 f_{ph}^\nu(r) + \mathcal{U}(\mathbf{r}) f_{ph}^\nu(r) - \int d^3 r' \mathcal{W}(\mathbf{r}, \mathbf{r}') f_{ph}^\nu(r') \\ &= \mathcal{H} [f_{ph}^\nu(r)]. \end{aligned} \quad (24)$$

In the above equation we have indicated with  $\nabla^2$  the usual Laplace operator where the differential terms related to  $\theta$  and  $\phi$  have been already applied to the spherical harmonics providing the correct eigenvalue. Therefore, in our writing, we imply that only the derivations on  $r$  should be done.

The operations described above are applied to all the terms of Eqs. (11) and (12). As example of our calculations, we write the contribution of the first interaction term of Eq. (11):

$$\begin{aligned} \oint_{\epsilon_p} R_p(r, \epsilon_p) \sum_{p'h'} \oint_{\epsilon_{p'}} v_{ph,p'h'}^J(\epsilon_p, \epsilon_{p'}) X_{p'h'}^\nu(\epsilon_{p'}) &= \\ &= \oint_{\epsilon_p} R_p(r, \epsilon_p) \sum_{p'h'} \oint_{\epsilon_{p'}} \int dr_1 r_1^2 \int dr_2 r_2^2 R_p^*(r_1, \epsilon_p) R_{h'}^*(r_2) \\ &\quad \left[ V_{ph,p'h'}^{J,\text{dir}}(r_1, r_2) R_h(r_1) R_{p'}(r_2, \epsilon_{p'}) - V_{ph,p'h'}^{J,\text{exc}}(r_1, r_2) R_{p'}(r_1, \epsilon_{p'}) R_h(r_2) \right] X_{p'h'}^\nu(\epsilon_{p'}) \\ &= \oint_{\epsilon_p} R_p(r, \epsilon_p) \sum_{p'h'} \int dr_1 r_1^2 \int dr_2 r_2^2 R_p^*(r_1, \epsilon_p) R_{h'}^*(r_2) \\ &\quad \left[ V_{ph,p'h'}^{J,\text{dir}}(r_1, r_2) R_h(r_1) f_{p'h'}^\nu(r_2) - V_{ph,p'h'}^{J,\text{exc}}(r_1, r_2) f_{p'h'}^\nu(r_1) R_h(r_2) \right] \\ &= \sum_{p'h'} \int dr_2 r_2^2 R_{h'}^*(r_2) \\ &\quad \left[ V_{ph,p'h'}^{J,\text{dir}}(r, r_2) R_h(r) f_{p'h'}^\nu(r_2) - V_{ph,p'h'}^{J,\text{exc}}(r, r_2) f_{p'h'}^\nu(r) R_h(r_2) \right] + \mathcal{T}(r), \end{aligned} \quad (25)$$

In the above equation we have used the definition (21) and the closure relation (8) and we have defined the term

$$\begin{aligned} \mathcal{T}(r) &= - \sum_{\epsilon_i < \epsilon_F} \delta_{ip} R_i(r) \int dr_1 r_1^2 R_i^*(r_1) \int dr_2 r_2^2 \sum_{p'h'} R_{h'}^*(r_2) \\ &\quad \left[ V_{ph,p'h'}^{J,\text{dir}}(r_1, r_2) R_h(r_1) f_{p'h'}^\nu(r_2) - V_{ph,p'h'}^{J,\text{exc}}(r_1, r_2) f_{p'h'}^\nu(r_1) R_h(r_2) \right], \end{aligned} \quad (26)$$

where, to simplify the writing, we have dropped the dependence of  $f$  on  $\nu \equiv (J, \Pi, \omega)$ .

We write a new set of CRPA secular equations where the unknowns are the channel functions  $f$  and  $g$ ,

$$\mathcal{H} [f_{ph}(r)] - (\epsilon_h + \omega) f_{ph}(r) = -\mathcal{F}_{ph}^J(r) + \sum_{\epsilon_i < \epsilon_F} \delta_{ip} R_i(r) \int dr_1 r_1^2 R_i^*(r_1) \mathcal{F}_{ph}^J(r_1), \quad (27)$$

$$\mathcal{H} [f_{ph}(r)] - (\epsilon_h - \omega) g_{ph}(r) = -\mathcal{G}_{ph}^J(r) + \sum_{\epsilon_i < \epsilon_F} \delta_{ip} R_i(r) \int dr_1 r_1^2 R_i^*(r_1) \mathcal{G}_{ph}^J(r_1), \quad (28)$$

where we have defined

$$\begin{aligned} \mathcal{F}_{ph}^J(r) = & \sum_{p'h'} \int dr_2 r_2^2 \\ & \left\{ R_{h'}^*(r_2) \left[ V_{ph,p'h'}^{J,\text{dir}}(r, r_2) R_h(r) f_{p'h'}(r_2) - V_{ph,p'h'}^{J,\text{exc}}(r, r_2) f_{p'h'}(r) R_h(r_2) \right] \right. \\ & \left. + g_{p'h'}^*(r_2) \left[ U_{ph,p'h'}^{J,\text{dir}}(r, r_2) R_h(r) R_{h'}(r_2) - U_{ph,p'h'}^{J,\text{exc}}(r, r_2) R_{h'}(r) R_h(r_2) \right] \right\}, \end{aligned} \quad (29)$$

and  $\mathcal{G}_{ph}^J$  is obtained from the above equation by interchanging the  $f$  and  $g$  channel functions. The relation between the  $U$  and  $V$  symbols is analogous to that of the  $u$  and  $v$  symbols of Eq. (14). The last terms in the right-hand side of Eqs. (27) and (28) are zero if there are no hole states having the same angular momenta  $l$  and  $j$  of the particle state considered.

We have changed a set of algebraic equations with unknowns depending on the continuous variable  $\epsilon_p$  into a set of integro-differential equations with unknowns depending on the distance from the center of coordinates. The solution of this problem requires to impose the proper boundary conditions. If the excitation energy  $\omega$  is above the nucleon emission threshold, in some of the  $ph$  excitation pairs compatible with the angular momentum and the parity of the final state, the particle has positive energy. We call open channels these  $ph$  pairs, and closed channels those pairs where the particle is in a discrete state.

After fixing the angular momentum  $J$  and the parity  $\Pi$  of the excited state, for each value of the excitation energy  $\omega$ , we solve Eqs. (27) and (28) a number of times equal to the number of the open channels. Every time we impose a different boundary condition, i.e. that the particle is emitted only in a specific channel, which we call elastic channel and we label it as  $p_0 h_0$ . For an open  $ph$  channel, we impose that the outgoing asymptotic behaviour of the channel function  $f_{ph}^{p_0 h_0}$  is

$$f_{ph}^{p_0 h_0}(r \rightarrow \infty) \rightarrow R_{p_0}(r, \epsilon_p) \delta_{p,p_0} \delta_{h,h_0} + \lambda H_p^-(\epsilon_h + \omega, r), \quad (30)$$

where  $\lambda$  is a complex normalization constant and  $H_p^-(\epsilon_h + \omega, r)$  is an ingoing Coulomb function or a Hankel function in case of a proton or neutron channel, respectively. The s.p. wave function  $R_p$  is eigenfunction of the HF hamiltonian (1) for positive energy, and is calculated as described in Appendix B.

In the case of a closed channel, the asymptotic behaviour is given by a decreasing exponential function

$$f_{ph}^{p_0 h_0}(r \rightarrow \infty) \rightarrow \frac{1}{r} \exp \left[ -r \left( \frac{2m|\epsilon_h + \omega|}{\hbar^2} \right)^{\frac{1}{2}} \right], \quad (31)$$

as in the case of the channel functions  $g_{ph}^{p_0 h_0}$ ,

$$g_{ph}^{p_0 h_0}(r \rightarrow \infty) \rightarrow \frac{1}{r} \exp \left[ -r \left( \frac{2m|\epsilon_h - \omega|}{\hbar^2} \right)^{\frac{1}{2}} \right]. \quad (32)$$

We solve the CRPA secular equations (27) and (28) by using a procedure similar to that presented in Ref. [29]. The channel functions  $f$  and  $g$  are expanded on a basis of sturmian functions  $\Phi_p^\mu$  which obey the required boundary conditions (30)-(32).

The sturmian functions  $\Phi_p^\mu$  are defined as eigenstates of the differential equation [34–38]

$$\left[ -\frac{\hbar^2}{2m} \frac{d^2}{dr^2} - \frac{\hbar^2}{m} \frac{1}{r} \frac{d}{dr} + \frac{\hbar^2}{2m} \frac{l_p(l_p+1)}{r^2} - \epsilon_p \right] \Phi_p^\mu(r) = -\overline{U}_p^\mu(r) \Phi_p^\mu(r), \quad (33)$$

where  $m$  is the particle mass,  $l_p$  is the orbital quantum number and  $\overline{U}_p^\mu(r)$  is a complex square well potential of the form

$$\overline{U}_p^\mu(r) = \begin{cases} \beta_p^\mu + i\gamma_p^\mu, & \text{if } r \leq a, \\ 0, & \text{if } r > a, \end{cases} \quad (34)$$

with  $\beta_p^\mu$  and  $\gamma_p^\mu$  real constants. The requirement of continuity of  $\Phi_p^\mu$  at  $r = a$  implies that only a discrete set of values of  $\beta_p^\mu$  and  $\gamma_p^\mu$  should be considered. In this set of solutions, the index  $\mu$  is related to the number of nodes of the

Sturm-Bessel function  $\Phi_p^\mu$  in the region  $0 \leq r \leq a$ . When the value of the index  $\mu$  increases by one unity, an additional node appears in the wave function at  $r \leq a$ . The definition of the Sturm-Bessel functions given above implies the orthogonality relation

$$(\beta_p^\mu + i\gamma_p^\mu) \int_0^a dr r^2 \Phi_p^\mu(r) \Phi_p^\nu(r) = \delta_{\mu\nu}. \quad (35)$$

Since, in general, the Sturm-Bessel functions are not orthogonal to the wave functions of the s.p. hole states, we find more useful to consider a set of orthogonalized functions which we construct as

$$\tilde{\Phi}_p^\mu(r) = \Phi_p^\mu(r) - \sum_{\epsilon_i < \epsilon_F} \delta_{ip} R_i^*(r) \int dr' r'^2 R_i(r') \Phi_p^\mu(r'), \quad (36)$$

where with  $\delta_{ip}$  we indicate that in the sum  $l_i = l_p$  and  $j_i = j_p$ . By using this set of orthogonalized sturmian functions we express the channel functions  $f_{ph}^{p_0 h_0}$  and  $g_{ph}^{p_0 h_0}$  as

$$f_{ph}^{p_0 h_0}(r) = R_{p_0}(r, \epsilon_{p_0}) \delta_{pp_0} \delta_{hh_0} + \sum_\mu c_{ph}^{\mu+} \tilde{\Phi}_p^{\mu+}(r), \quad (37)$$

$$g_{ph}^{p_0 h_0}(r) = \sum_\mu c_{ph}^{\mu-} \tilde{\Phi}_p^{\mu-}(r), \quad (38)$$

where the superscripts  $+$  and  $-$  indicate that the sturmian functions are calculated for  $\epsilon_p = \epsilon_h + \omega$  or  $\epsilon_p = \epsilon_h - \omega$  respectively. To simplify the writing we drop the explicit dependence on the open channel label  $p_0 h_0$  of all the  $c_{ph}^\mu$  expansion coefficients.

We insert the expressions (37) and (38) in the secular equations (27) and (28), and following the steps presented in Appendix A, we obtain a system of linear equations whose unknowns are the expansion coefficients  $c_{ph}^{\mu\pm}$ . The new CRPA secular equations are

$$\begin{aligned} \sum_\mu \sum_{p'h'} \left\{ \left[ \delta_{pp'} \delta_{hh'} \left( \delta_{\mu\nu} - \langle (\Phi_p^{\nu+})^* | \mathcal{U} | \Phi_p^{\mu+} \rangle + \langle (\Phi_p^{\nu+})^* | \mathbb{I} | \mathcal{W} | \mathbb{I} | \Phi_p^{\mu+} \rangle \right) \right. \right. \\ \left. \left. + \sum_{\epsilon_i < \epsilon_F} \delta_{ip} (\epsilon_i - \epsilon_h - \omega) \langle (\Phi_p^{\nu+})^* | R_i \rangle \langle (R_i)^* | \Phi_p^{\mu+} \rangle \right) \right. \\ \left. - \left( \langle (\tilde{\Phi}_p^{\nu+})^* R_{h'} | V_{ph,p'h'}^{J,\text{dir}} | R_h \tilde{\Phi}_{p'}^{\mu+} \rangle - \langle (\tilde{\Phi}_p^{\nu+})^* R_{h'} | V_{ph,p'h'}^{J,\text{exc}} | \tilde{\Phi}_{p'}^{\mu+} R_h \rangle \right) \right] c_{p'h'}^{\mu+} \\ \left. - \left( \langle (\tilde{\Phi}_p^{\nu+})^* \tilde{\Phi}_{p'}^{\mu-} | U_{ph,p'h'}^{J,\text{dir}} | R_h R_{h'} \rangle - \langle (\tilde{\Phi}_p^{\nu+})^* \tilde{\Phi}_{p'}^{\mu-} | U_{ph,p'h'}^{J,\text{exc}} | R_{h'} R_h \rangle \right) (c_{p'h'}^{\mu-})^* \right\} = \\ = \langle (\tilde{\Phi}_p^{\nu+})^* R_{h_0} | V_{ph,p_0 h_0}^{J,\text{dir}} | R_h R_{p_0}(\epsilon_{p_0}) \rangle - \langle (\tilde{\Phi}_p^{\nu+})^* R_{h_0} | V_{ph,p_0 h_0}^{J,\text{exc}} | R_{p_0}(\epsilon_{p_0}) R_h \rangle, \end{aligned} \quad (39)$$

$$\begin{aligned} \sum_\mu \sum_{p'h'} \left\{ \left[ \delta_{pp'} \delta_{hh'} \left( \delta_{\mu\nu} - \langle (\Phi_p^{\nu-})^* | \mathcal{U} | \Phi_p^{\mu-} \rangle + \langle (\Phi_p^{\nu-})^* | \mathbb{I} | \mathcal{W} | \mathbb{I} | \Phi_p^{\mu-} \rangle \right) \right. \right. \\ \left. \left. + \sum_{\epsilon_i < \epsilon_F} \delta_{ip} (\epsilon_i - \epsilon_h + \omega) \langle (\Phi_p^{\nu-})^* | R_i \rangle \langle (R_i)^* | \Phi_p^{\mu-} \rangle \right) \right. \\ \left. - \left( \langle (\tilde{\Phi}_p^{\nu-})^* R_{h'} | V_{ph,p'h'}^{J,\text{dir}} | R_h \tilde{\Phi}_{p'}^{\mu-} \rangle - \langle (\tilde{\Phi}_p^{\nu-})^* R_{h'} | V_{ph,p'h'}^{J,\text{exc}} | \tilde{\Phi}_{p'}^{\mu-} R_h \rangle \right) \right] c_{p'h'}^{\mu-} \\ \left. - \left( \langle (\tilde{\Phi}_p^{\nu-})^* \tilde{\Phi}_{p'}^{\mu+} | U_{ph,p'h'}^{J,\text{dir}} | R_h R_{h'} \rangle - \langle (\tilde{\Phi}_p^{\nu-})^* \tilde{\Phi}_{p'}^{\mu+} | U_{ph,p'h'}^{J,\text{exc}} | R_{h'} R_h \rangle \right) (c_{p'h'}^{\mu+})^* \right\} = \\ = \langle (\tilde{\Phi}_p^{\nu-})^* R_{p_0}(\epsilon_{p_0}) | U_{ph,p_0 h_0}^{J,\text{dir}} | R_h R_{h_0} \rangle - \langle (\tilde{\Phi}_p^{\nu-})^* R_{p_0}(\epsilon_{p_0}) | U_{ph,p_0 h_0}^{J,\text{exc}} | R_{h_0} R_h \rangle. \end{aligned} \quad (40)$$

In the above expressions, with the bra and ket integration convention we indicate integrations on radial variables only. The number of these integrations is given by the number of the functions inserted between the bra and ket symbols. For this reason we have inserted the symbol  $\mathbb{I}$  indicating the identity function.

Summarizing, we have converted the CRPA secular equations (11) and (12) into a set of algebraical equations whose unknowns are the expansion coefficients  $c_{ph}^\mu$ . These equations have a solution for each value of the excitation energy  $\omega$  above the nucleon emission threshold.

The solution of the secular CRPA equations provides the channel functions  $f$  and  $g$  and this allows us to calculate the transition matrix elements induced by an operator  $T_J$ . If the operator  $T_J$  inducing the transition is of one-body type of the form

$$T_{JM}(\mathbf{r}) = \sum_{i=1}^A F_J(r_i) \theta_{JM}(\Omega_i) \delta(\mathbf{r}_i - \mathbf{r}), \quad (41)$$

where we have separated the dependence on the radial and angular parts of the operator, we obtain for the transition matrix element the expression

$$\begin{aligned} \langle J \| T_J \| 0 \rangle_{p_0 h_0} = \sum_{ph} \left[ \langle j_p \| \theta_J \| j_h \rangle \int dr r^2 (f_{ph}^{p_0 h_0}(r))^* F_J(r) R_h(r) \right. \\ \left. + (-1)^{J+j_p-j_h} \langle j_h \| \theta_J \| j_p \rangle \int dr r^2 R_h^*(r) F_J(r) g_{ph}^{p_0 h_0}(r) \right], \end{aligned} \quad (42)$$

where with the double bar we indicate the reduced matrix elements of the angular coordinates, as defined in [33].

In this paper we present results regarding nuclear excitations induced by photons. We consider here only natural parity, electric, excitations, and we use the following expression for the operator  $T_J$

$$T_{JM} = \sum_{i=1}^A Z_i^{\text{eff}} r_i^J Y_{JM}(\Omega_i) \delta(\mathbf{r}_i - \mathbf{r}), \quad (43)$$

where  $Z_i^{\text{eff}}$  is the effective charge

$$Z_i^{\text{eff}} = \begin{cases} \left( \frac{N}{A} \right) \frac{1}{2} [1 + \tau_3(i)] - \left( \frac{Z}{A} \right) \frac{1}{2} [1 - \tau_3(i)], & \text{if } J^\Pi = 1^- \\ \frac{1}{2} [1 + \tau_3(i)], & \text{otherwise.} \end{cases} \quad (44)$$

The second of these expressions is obtained by using an approximation valid for the medium-heavy nuclei we are studying [39]. In the above equation  $A$ ,  $Z$  and  $N$  are the mass, proton and neutron numbers respectively, and  $\tau_3(i) = 1$  for protons and  $-1$  for neutrons. For a given excitation energy  $\omega$ , and electric transition  $EJ$ , we calculate the  $B$ -value as the incoherent sum on every open channel  $p_0 h_0$ ,

$$B(\omega, EJ : 0 \rightarrow J) = \sum_{p_0 h_0} |\langle \omega, J \| T_J \| 0 \rangle_{p_0 h_0}|^2. \quad (45)$$

We obtain the total photoabsorption cross section from the  $B$ -value by using the expression [40]

$$\sigma(\omega, 0 \rightarrow J) = 8\pi^3 \frac{J+1}{J} \frac{e^2}{[(2J+1)!!]^2} \left( \frac{\omega}{\hbar c} \right)^{2J-1} B(\omega, EJ : 0 \rightarrow J), \quad (46)$$

where we have indicated with  $e$  the elementary charge.

### III. DETAILS OF THE CALCULATIONS

The formalism developed in the previous section leads to a set of algebraic equations whose unknowns are the expansion coefficients  $c_{ph}^{\mu\pm}$ . The number of coefficients, and therefore the dimensions of the complex matrix to diagonalize, is an input of our approach.

Since the expansion on a basis of sturmian functions is a technical artifact, the solution of the CRPA secular equations must be independent of the number of expansion coefficients. We tested the convergence of our results by controlling the values of the total photoabsorption cross section in  $^{16}\text{O}$  and  $^{40}\text{Ca}$  nuclei. We reached the stability up



to the fifth significant figure with 10 expansion coefficients, independently of the multipolarity and of the energy of the excitation.

In our calculations we have used two different parameterizations of the Gogny interaction, the more traditional D1S force [41] and the new D1M force [42] obtained from a fit to about 2000 nuclear binding energies and 700 charge radii. The D1S and D1M forces describe the empirical saturation point of symmetric nuclear matter and reproduce rather well the behaviour of the equations of state calculated with microscopic approaches [43, 44]. The situation for pure neutron matter is different, because the behaviour of the D1S equation of state at high densities is unphysical. The D1M force produces an equation of state which has a plausible behaviour at higher densities, even though it does not reproduce the results of modern microscopic calculations.

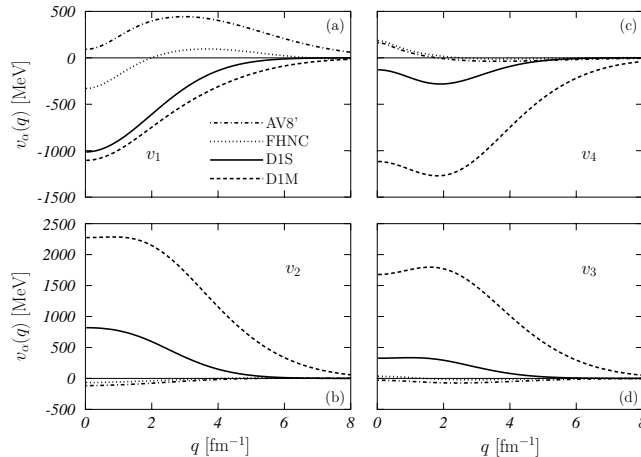


Figure 1: Comparison between the interactions used in our calculations and the microscopic Argonne V8' interaction in the scalar channel,  $v_1$ , spin channel,  $v_2$ , isospin channel,  $v_3$ , and in the spin-isospin channel,  $v_4$ . The dashed-dotted lines, labelled FHNC, have been obtained by multiplying the Argonne V8' terms with the scalar part of the correlation function obtained in Correlated Basis Function calculations [10].

In Fig. 1 we show the D1S and D1M forces in momentum space, and we compare them with the bare Argonne V8' interaction [3]. The scalar,  $v_1$  (panel (a)), isospin,  $v_2$  (panel (b)), spin,  $v_3$  (panel (c)) and spin-isospin,  $v_4$  (panel (d)), channels are shown. The dashed-dotted lines have been obtained by multiplying the Argonne V8' terms with the scalar part of the correlation function obtained in the finite nuclei Correlated Basis Function calculations of Ref. [10]. To be precise we have used the correlation function obtained for the  $^{48}\text{Ca}$  nucleus. In any case, these correlation functions are rather similar for all the nuclei considered (see Fig. 21 of Ref. [10]). The large differences between microscopic and effective interactions shown in Fig. 1 indicate that the effective interactions take into account a large number of effects explicitly treated in microscopic calculations. The effects originated by the short-range correlations are only a limited part of them. It is interesting to notice, in the spin, isospin and spin-isospin channels, the extremely large values of the D1M interaction, with respect to those of the other forces.

In the next section we shall compare self-consistent CRPA results with those of phenomenological calculations. The s.p. wave functions of the phenomenological calculations have been obtained by using Woods-Saxon wells, whose parameters are given in Ref. [10]. The residual interaction is a zero-range, density dependent, Landau-Migdal force whose parameters are those chosen in Ref. [45].

We have investigated nuclei where the hole s.p. levels are fully occupied. This eliminates deformations and minimizes pairing effects.

## IV. RESULTS

### A. Oxygen

We have studied three oxygen isotopes, the doubly magic  $^{16}\text{O}$  nucleus, and the  $^{22}\text{O}$  and  $^{24}\text{O}$  isotopes. In our model, the heavier isotopes are obtained from the  $^{16}\text{O}$  core by filling, respectively, the neutron  $1d_{5/2}$ , and the  $2s_{1/2}$  s.p. levels. The ground state properties of these three isotopes, obtained in HF calculations with the D1S and D1M interactions, are presented in Table I, and in Figs. 2 and 3.

	D1S			D1M		
	<sup>16</sup> O	<sup>22</sup> O	<sup>24</sup> O	<sup>16</sup> O	<sup>22</sup> O	<sup>24</sup> O
$E/A$	-8.093	-7.372	-7.012	-7.955	-7.254	-6.912
protons						
$1s_{1/2}$	-35.37	-46.43	-48.64	-32.74	-43.38	-45.65
$1p_{3/2}$	-18.58	-29.89	-32.32	-17.63	-28.71	-31.18
$1p_{1/2}$	-12.49	-23.99	-25.97	-11.91	-23.60	-25.60
neutrons						
$1s_{1/2}$	-38.61	-41.02	-41.11	-36.00	-38.32	-38.46
$1p_{3/2}$	-21.82	-22.11	-22.43	-20.91	-20.72	-21.15
$1p_{1/2}$	-15.63	-18.53	-17.22	-15.10	-17.35	-16.29
$1d_{5/2}$		-6.56	-7.01		-6.34	-6.85
$2s_{1/2}$			-4.13			-4.09

Table I: Nuclear binding energies per nucleon,  $E/A$ , and s.p. energies of the three oxygen isotopes we have considered, calculated within the HF approach by using the D1S and D1M interactions. All the quantities are expressed in MeV. The values of the experimental binding energies are -7.976, -7.365 and -7.016 MeV for <sup>16</sup>O, <sup>22</sup>O and <sup>24</sup>O, respectively.

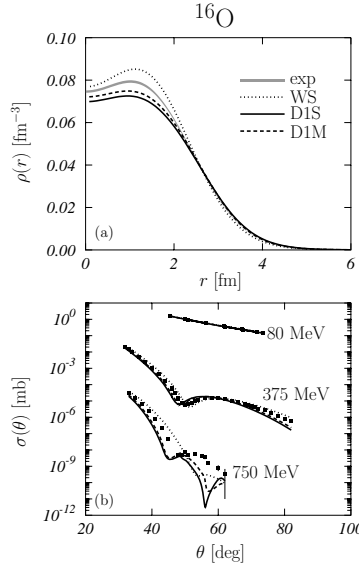


Figure 2: Panel (a): charge density distributions of the <sup>16</sup>O nucleus. The shaded area represents the empirical density distribution [46]. The other lines show the distributions obtained in HF calculations with the D1S and D1M interactions (full and dashed lines, respectively) and that obtained with the Woods-Saxon potential of Ref. [10] (dotted line). Panel (b): elastic electron scattering cross sections calculated in Distorted Wave Born Approximation by using the charge distributions shown in the upper panel, as a function of the scattering angle  $\theta$ . The empirical charge distribution plotted in the upper panel (dashed-dotted line) has been obtained from a fit to the data taken from Ref. [48, 49]. The numbers in the panel indicate the values of the electron energy.

We show in Table I the binding energies per nucleon,  $E/A$ , and the s.p. energies of the three oxygen isotopes. The agreement with the experimental binding energies, whose values are given in the table caption, is within the few percent. We observe that the D1M interaction is slightly less attractive than the D1S one. In any case, these are relatively small differences and we may state that, despite the fact that the two interactions are rather different, as we have shown in Fig. 1, they give very similar descriptions of the binding and s.p. energies of the three nuclei considered. The results of the table show that the proton s.p. states become more bound with the increasing of the number of neutrons.

In the panel (a) of Fig. 2 we show the <sup>16</sup>O charge distributions obtained in HF calculations where the D1S and D1M forces have been used, and we compare them with the empirical charge distribution taken from Ref. [46]. Our charge

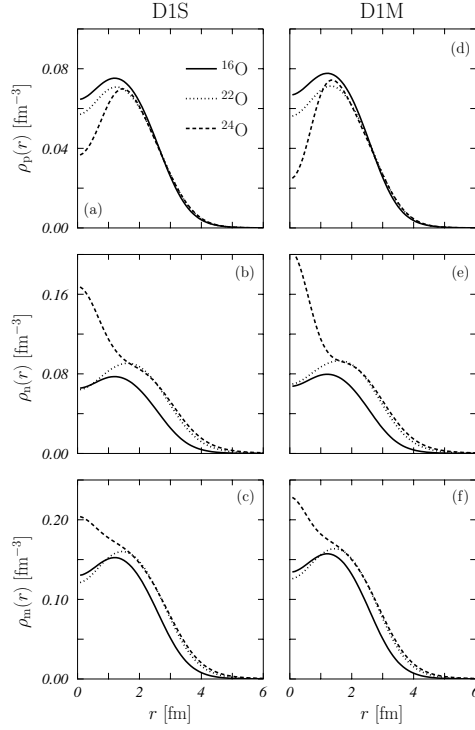


Figure 3: Proton  $\rho_p$ , neutron  $\rho_n$  and matter  $\rho_m$  distributions for the three oxygen isotopes we have considered, obtained in HF calculations with the D1S and D1M interactions.

distributions have been obtained by folding the proton distributions with a dipole proton electromagnetic form factor. We have verified that more modern, and accurate, form factors do not produce sizable differences in our results. Our calculations describe well the empirical charge density on the surface but they underestimate it in the center of the nucleus. We show in panel (b) of Fig. 2 the elastic electron scattering cross section calculated in Distorted Wave Born Approximation [47] by using the charge distributions shown in the panel (a). We compared our results with the data of Ref. [48, 49]. The differences between theoretical and empirical densities show up in the cross sections at large momentum transfer. The charge distribution obtained with the Woods-Saxon potential by using the parameters of Ref. [10], does not make a better job in describing the empirical density, which is now overestimated in the nuclear center.

In Fig. 3, we show the proton, neutron, and matter distributions,  $\rho_p$ ,  $\rho_n$  and  $\rho_m$  respectively, for the three oxygen isotopes we have considered. The matter distribution is the sum of the proton and neutron ones. We do not remark relevant differences between the results obtained with the two different interactions. The shapes of the neutron distributions show the effects of the filling of the s.p. levels, which are empty in the lighter isotopes. In the <sup>22</sup>O nucleus the  $1d_{5/2}$  level, empty in <sup>16</sup>O, is completely occupied. This level gives a contribution mainly on the surface. The rms radius of the neutron distribution changes from 2.64 fm in <sup>16</sup>O to 3.00 fm in <sup>22</sup>O, for the D1S interaction, and from 2.61 fm to 2.97 fm for the D1M interaction. The situation is different in <sup>24</sup>O, where the new s.p. level to be occupied is the  $2s_{1/2}$ . In this case, the main effect is in the center of the nucleus. The values of the neutron distributions rms radii are 3.17 fm and 3.12 fm for the D1S and D1M interaction respectively. It is a relatively small change on the neutron distribution surface.

The proton distributions are interesting since there is no change in the occupation of the s.p. levels in the different isotopes, therefore all the differences are produced by the interaction between protons and neutrons. In the panels (a) and (d) of Fig. 3 we show the proton distributions of the three oxygen isotopes. We notice that the increase of the neutron number produces a change in the interior of the nucleus. The proton  $1s_{1/2}$  s.p. wave function becomes wider the heavier is the isotope, and since the normalization is conserved, the value of wave function at the center of the nucleus becomes smaller. The rms radius of these distributions changes from 2.20 fm in <sup>16</sup>O to 2.45 fm in <sup>24</sup>O almost independently of the interaction used. The relevant lowering of the proton distribution in the nuclear center is produced to compensate the increase of the neutron density (see panels (b) and (e)). In the panels (c) and (f) we also show the matter distributions and we observe that the differences between the various isotopes are smaller than those shown separately by the proton and neutron distributions.

So far, we have presented HF results which are related to the ground states properties of the three oxygen isotopes. We discuss now the excitation spectra obtained by our CRPA calculations. A first point we have investigated is related to the relevance of the proper treatment of the continuum in the self-consistent CRPA calculations. Our study has been conducted by comparing our CRPA results with the results of discrete RPA calculations, such as those of Ref. [27]. This is the same strategy adopted in Ref. [30] and, within a relativistic framework, in Ref. [50]. The discrete set of s.p. states is obtained by solving the HF equations in a box with bound state boundary conditions. For all oxygen isotopes we use a box radius of 12 fm. Larger values of this radius do not change binding and s.p. energies up to the fifth significant figure. There is not such a stability for the unbound,  $\epsilon_p > 0$ , s.p. wave functions and energies. We have controlled the stability of the RPA results by selecting the maximum value of the particle-hole excitation energy,  $\epsilon_{ph}^{\max}$ , used in the RPA calculation. For a given total angular momentum and parity of the excitation, this value determines the number of s.p. states forming the configuration space of the discrete calculation.

The quantity we have considered for these convergence tests is the centroid energy, which we calculate as

$$\langle \omega \rangle_J = \frac{\int_{\omega_{\min}}^{\omega_{\max}} d\omega \omega B(\omega, EJ : 0 \rightarrow J)}{\int_{\omega_{\min}}^{\omega_{\max}} d\omega B(\omega, EJ : 0 \rightarrow J)}. \quad (47)$$

We have studied the convergence for the  $1^-$  and  $2^+$  excitations in all the nuclei we have investigated, and we have found that the change from  $\epsilon_{ph}^{\max}=200$  MeV to  $\epsilon_{ph}^{\max}=250$  MeV modifies the value of the centroid energies for less than one part on a thousand. All the discrete RPA results we present here have been obtained by using  $\epsilon_{ph}^{\max}=250$  MeV. Our choice ensures the convergence of discretized RPA calculations done with HF basis which has been generated by using a specific value of the box size.

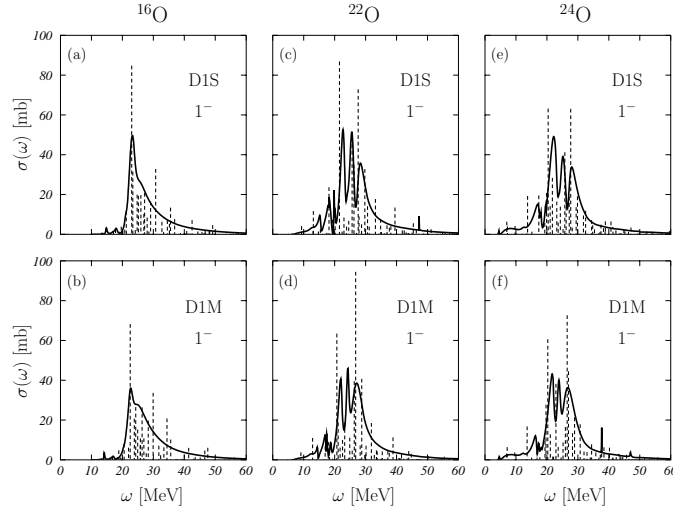


Figure 4: Total photoabsorption cross sections calculated with discrete and continuum RPA approaches. The vertical bars show the discrete results, and the solid lines those of the CRPA calculations. The excitation multipole is the  $1^-$ . The upper panels show the results obtained with the D1S interaction, the lower panels with the D1M interaction.

In Fig. 4 we compare the total photoabsorption cross sections calculated for the excitation of the  $1^-$  resonance in the three oxygen isotopes we have studied. The vertical bars show the discrete RPA results and the solid lines those of the CRPA calculations. In the upper panels we present the results obtained with the D1S interaction, and in the lower panels those obtained with the D1M interaction.

In the  $^{16}\text{O}$  nucleus, the agreement between the results of the two different calculations is rather good. Discrete results have their maxima in the same position of those of the continuous solutions. There are peaks around 30, 35 and 40 MeV which do not have corresponding partners in the CRPA cross sections. The D1M cross sections are slightly smaller, indicating, again, that this interaction is less attractive than the D1S force. The situation is more complicated in  $^{22}\text{O}$ . Discrete and continuum results have similar structures, but the positions of the peaks are slightly different. In any case, the cross sections show a richer structure than in the  $^{16}\text{O}$  case. This situation is worsening in  $^{24}\text{O}$  where the peaks of the continuous cross sections do not correspond to those of the discrete calculation.

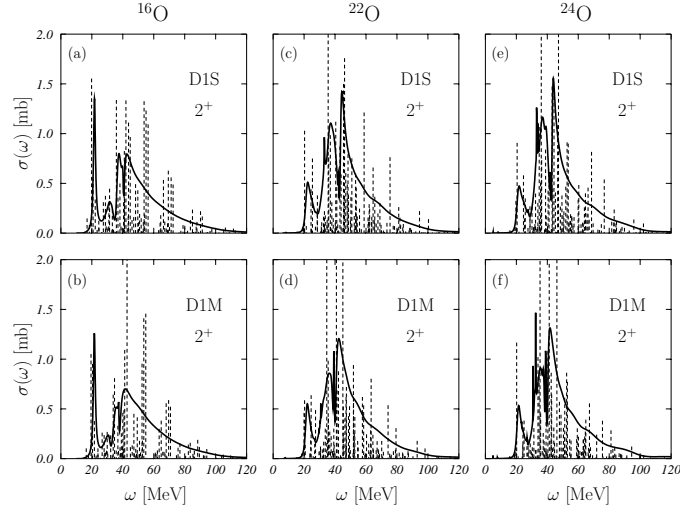


Figure 5: The same as Fig. 4 for the  $2^+$  multipole excitation.

We show in Fig. 5 analogous results for the excitation of the  $2^+$  resonance. In this case the results of the discrete RPA are rather different from those of the CRPA, even in the  $^{16}\text{O}$  nucleus. The discrete calculations show clusters of peaks not present in the continuous calculations.

	$^{16}\text{O}$	$^{22}\text{O}$	$^{24}\text{O}$
$1^-$			
RPA-D1S	26.34	24.87	22.82
CRPA-D1S	27.17	25.11	23.07
RPA-D1M	26.36	24.72	22.81
CRPA-D1M	27.23	25.04	23.20
$2^+$			
RPA-D1S	28.43	32.91	31.58
CRPA-D1S	30.47	33.47	32.20
RPA-D1M	28.19	32.26	30.93
CRPA-D1M	30.51	33.06	31.06

Table II: Centroid energies in MeV, Eq. (47), for the  $1^-$  and  $2^+$  electromagnetic excitations in the three oxygen isotopes we have studied, obtained with discrete (RPA) and continuum (CRPA) calculations.

We show in Table II the centroid energies of the electromagnetic responses obtained in discrete and continuum RPA calculations. We have considered for  $\omega_{\min}$  the values corresponding to the continuum thresholds. The  $1^-$  resonances have been integrated up to  $\omega_{\max} = 60$  MeV, while the  $2^+$  resonances up to  $\omega_{\max} = 120$  MeV. The relative differences between these centroid energies are smaller than 2% in the  $1^-$  case. In the case of the  $2^+$  excitation we reach the maximum value of 4% relative difference between the D1M results in  $^{16}\text{O}$ .

While the  $1^-$  response to photon excitations is essentially of pure isovector character, the  $2^+$  response is a combination of isoscalar (IS) and isovector (IV) modes. For the  $2^+$  excitation we have separated the IS and IV responses by including in the expression of the  $B(EJ)$  value of Eq. (45) the operators

$$T_{JM}^{IS} = \sum_{i=1}^A r_i^J Y_{JM}(\Omega_i) \quad (48)$$

$$T_{JM}^{IV} = \sum_{i=1}^A r_i^J Y_{JM}(\Omega_i) \tau_3(i) \quad (49)$$

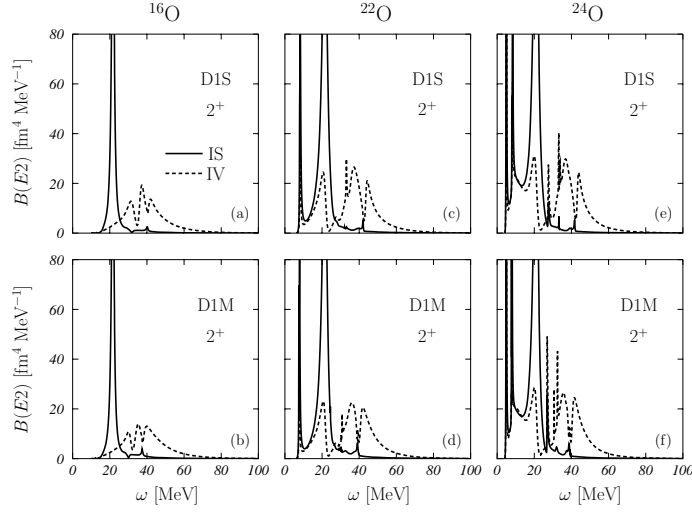


Figure 6: Isoscalar (IS) and isovector (IV) strengths of the  $2^+$  excitation mode for the oxygen isotopes we have studied.

with  $J = 2$ . We show in Fig. 6 the IS and IV responses for the  $2^+$  excitation of all the three oxygen isotopes we have investigated obtained by using the D1S and the D1M interactions. The IS responses are concentrated at lower energies and show a sharp peak, while the IV responses are broader and they have less pronounced maxima at higher energies. In the  $^{16}\text{O}$  nucleus the IS quadrupole resonance has been identified in  $\alpha$  scattering processes at a peak energy of about 21 MeV [51], to be compared with the peak energies of 21.7 and 21.6 MeV obtained with the D1S and D1M forces respectively. The centroid energies of our calculations for the  $^{16}\text{O}$  nucleus, calculated for  $\omega_{\text{max}}=100$  MeV are 22.94 and 23.13 MeV for D1S and D1M interactions respectively. If we consider  $\omega_{\text{max}}=40$  MeV we obtain 22.12 and 22.24 MeV for these centroid energies.

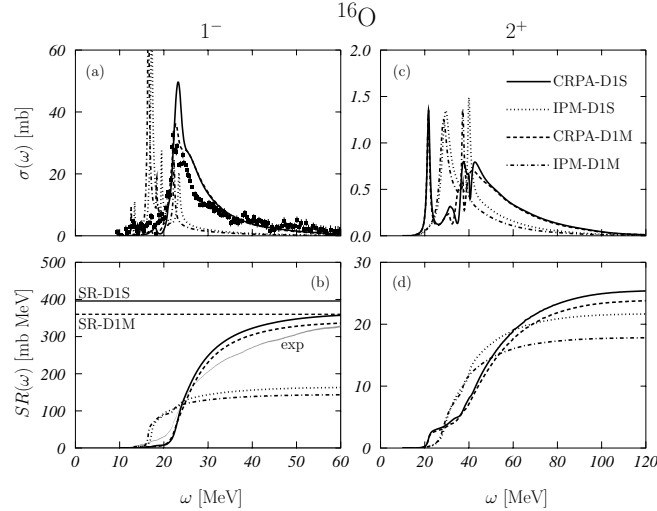


Figure 7: Total photoabsorption cross sections for the  $1^-$  (panel (a)) and  $2^+$  (panel (c)) excitations. Experimental data (solid squares) are from Ref. [52]. In panels (b) and (d), we show the sum rule exhaustion functions, Eq. (50), for the two multipole excitations. The grey area indicates the same function calculated for the experimental data. Full and dashed lines show the CRPA results obtained with the D1S and D1M interactions, respectively, and the dotted and dashed-dotted lines the IPM results obtained with the D1S and D1M HF single particle wave functions, respectively. The horizontal lines indicate the sum rule limiting values obtained by using a nuclear matter estimate of the enhancement factor. The values of the TRK sum rule is 240 mb MeV.

Another point we have investigated is related to the effects of the residual interaction in CRPA calculations. In Fig. 7 the CRPA results (solid and dashed curves) are compared with the IPM results (dotted and dashed-dotted curves),

obtained by switching off the residual interaction in the CRPA calculation, and with the data of Ref. [52]. Since more than the 90% of the contribution to the total photoabsorption cross section is given by the  $1^-$  excitation, we compare the data with results of this excitation mode. The contribution of the  $2^+$  excitation to the photoabsorption cross section is shown in the panel (c) of the figure, and it is one order of magnitude smaller than the contribution of the  $1^-$  mode. In the lower panels we present the sum rule exhaustion functions,

$$SR(\omega) = \int_0^\omega d\omega' \sigma(\omega'), \quad (50)$$

calculated for the cross sections shown in the upper panels.

The results obtained with the D1S interaction do not show significant differences with respect to those obtained with the D1M interaction. Evidently, only the CRPA calculations predict the presence, and also the positions, of the resonances. The positions of the peaks are well reproduced for both multipole excitations by the CRPA calculations, while the IPM results do not give a good description of the data. The sum rule functions obtained with the IPM calculations are smaller than those of the CRPA. The differences are larger for the  $1^-$  excitation than for the  $2^+$  excitation. This may be due to the different isospin character of the two excitations, which, as we have already pointed out, is mainly IV in the  $1^-$  mode, and a combination of IS and IV in the  $2^+$  mode. In the  $1^-$  case, the energies of the peaks of the CRPA cross sections are larger than those of the IPM results. This because the residual interactions are repulsive in the isovector channel. The situation is inverted for the lower energy peaks of the  $2^+$  excitation mode. The CRPA cross sections present peaks at lower energies than those of the IPM calculations. This indicates that the interactions are attractive in the isoscalar channel. The other, wider,  $2^+$  resonances peaked at energies of about 42 MeV, have, instead, IV character, and their energies are slightly greater than those of the IPM ones.

The comparison of the CRPA results with the photoabsorption data emphasizes the well known limitations of the RPA description of the giant resonances. The strength is too concentrated in the peak region, and the data show a wider energy distribution. The sum rule functions of the panel (b) of Fig. 7 further confirm these deficiencies. Even though experimental and CRPA curves seem to have the same limiting values, the CRPA curves saturate much earlier than the experimental one. Again, the strength is too concentrated in the resonance region.

The saturation value given by the Thomas-Reiche-Kuhn (TRK) sum rule is of 240 mb MeV. The isospin dependence of our interactions is responsible for the fact that our calculations saturate at higher values. The calculation of the enhancement factor  $\kappa$  of the TRK sum rule is rather involved for finite-range interactions [53]. We use the values of  $\kappa$  for the D1S and D1M interactions obtained by a nuclear matter estimate [30]. We obtain  $\kappa=0.65$  for the D1S interaction and  $\kappa=0.50$  for the D1M force. These values correspond in  $^{16}\text{O}$  to sum rule limiting values of 396 and 360 mb MeV for the D1S and D1M interaction respectively. As we show in the panel (b) of Fig. 7, these values are compatible with the results we obtain with our CRPA calculations.

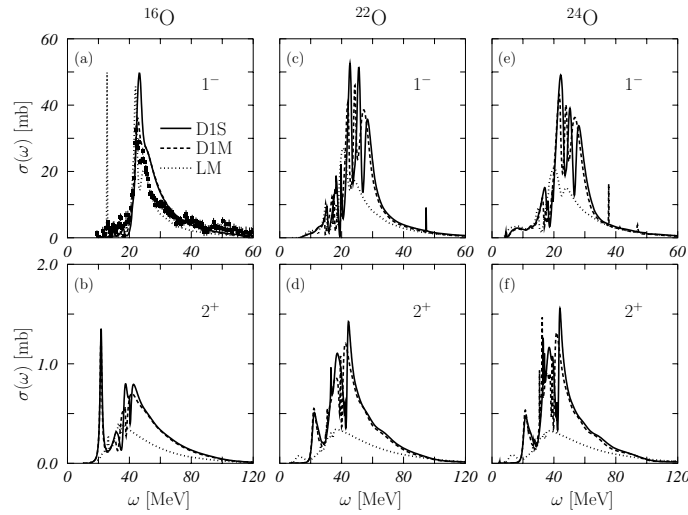


Figure 8: Comparison between the self-consistent CRPA results obtained with the D1S interaction (full lines), the D1M interaction (dashed lines) and those obtained with the phenomenological approach of Refs. [54, 55] where a Landau-Migdal interaction has been used (dotted lines).

Another issue we have investigated is the capacity of a phenomenological CRPA approach to predict the excitation spectra of experimentally unknown nuclei. For this reason we have calculated the  $1^-$  and  $2^+$  excitations of the three

	D1S			D1M		
	<sup>40</sup> Ca	<sup>48</sup> Ca	<sup>52</sup> Ca	<sup>40</sup> Ca	<sup>48</sup> Ca	<sup>52</sup> Ca
$E/A$	-8.579	-8.639	-8.344	-8.462	-8.537	-8.260
protons						
$1s_{1/2}$	-44.82	-51.31	-54.01	-41.01	-46.90	-49.35
$1p_{3/2}$	-30.04	-37.61	-40.02	-27.84	-34.91	-37.16
$1p_{1/2}$	-26.05	-33.89	-35.76	-24.14	-31.74	-33.60
$1d_{5/2}$	-16.02	-23.89	-26.37	-15.15	-22.65	-25.07
$2s_{1/2}$	-10.52	-17.12	-20.93	-9.91	-16.17	-19.98
$1d_{3/2}$	-9.18	-16.96	-19.29	-8.75	-16.54	-18.82
neutrons						
$1s_{1/2}$	-52.07	-53.20	-53.14	-48.44	-49.57	-49.52
$1p_{3/2}$	-37.09	-37.89	-37.88	-35.00	-35.60	-35.71
$1p_{1/2}$	-33.01	-35.32	-34.46	-31.21	-33.23	-32.56
$1d_{5/2}$	-22.96	-22.92	-23.09	-22.15	-21.84	-22.13
$2s_{1/2}$	-17.54	-18.27	-17.40	-17.03	-17.69	-17.89
$1d_{3/2}$	-15.95	-17.83	-18.85	-15.57	-17.09	-16.83
$1f_{7/2}$		-9.39	-9.76		-9.25	-9.71
$2p_{3/2}$			-5.49			-5.50

Table III: Nuclear binding energies per nucleon,  $E/A$ , and s.p. energies of the three calcium isotopes we have considered, calculated within the HF approach by using the D1S and D1M interactions. All the quantities are expressed in MeV. The values of the experimental binding energies are -8.551, -8.666 and -8.396 MeV for <sup>40</sup>Ca, <sup>48</sup>Ca and <sup>52</sup>Ca, respectively.

oxygen isotopes by using the phenomenological approach of Refs. [54, 55]. In the phenomenological calculations we solved the CRPA equations without exchange terms by using a zero-range Landau-Migdal force, whose parameters are those of Ref. [45]. In this approach the s.p. wave functions are generated by solving the one-body Schrödinger equation with a Woods-Saxon potential. For all the oxygen isotopes, we used the parameters of the Woods-Saxon potential of <sup>16</sup>O given in [10]. In Fig. 8 we compare our self-consistent CRPA results with those of the phenomenological approach which are indicated by the dotted lines.

The phenomenological results compare rather well with experimental data [52] and with our self-consistent CRPA results in the case of the  $1^-$  excitation of the <sup>16</sup>O nucleus. The position of the peak coincides with that obtained in the self-consistent calculations, and all of them are rather close to the experimental one. We remark, however, that the global strength of the phenomenological result is smaller than that produced in the self-consistent approach. The reasonable agreement between the CRPA results obtained in the case of the  $1^-$  excitation in <sup>16</sup>O is peculiar since all the other cases show large differences between phenomenological and self-consistent results. The phenomenological calculation predicts the isoscalar  $2^+$  excitation of <sup>16</sup>O at 21 MeV energy, but it fails in describing the isovector excitation at higher energies. The differences between the results of the phenomenological and self-consistent calculations in the other two oxygen isotopes are large. The total strengths of the phenomenological cross sections are much smaller than those of the self-consistent ones. Great part of the resonance structure of the self-consistent cross sections is absent in the phenomenological results.

## B. Calcium

The same type of investigation done for the oxygen isotopes has been repeated for three calcium isotopes: <sup>40</sup>Ca, <sup>48</sup>Ca and <sup>52</sup>Ca. The ground state properties of these nuclei are presented in Table III and in Figs. 9 and 10. In Table III we give the values of the binding and s.p. energies. As in case of oxygen, the agreement with the experimental binding energies is within few percents. To be precise, we remark that the D1S results are slightly better than those obtained with the D1M force. Also in these calculations the D1M force shows less attraction than the D1S interaction. As in the case of oxygen, the proton s.p. levels become more bound with increasing number of neutrons.

In the upper panels of Fig. 9 we show the charge distributions of <sup>40</sup>Ca and <sup>48</sup>Ca nuclei. We use these charge distributions to calculate in Distorted Wave Born Approximation the elastic electron scattering cross sections. These cross sections are compared with the experimental data [49, 56–59] in the lower panels of the figure. In the figure we



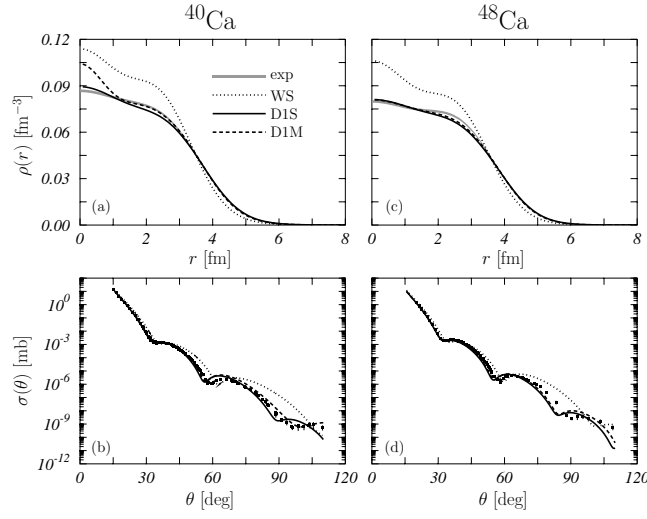


Figure 9: The same as Fig. 2 for the  $^{40}\text{Ca}$  and  $^{48}\text{Ca}$  nuclei. The empirical densities are taken from the compilation of Ref. [46]. The elastic electron scattering data on  $^{40}\text{Ca}$  from Refs. [56–58], and those of  $^{48}\text{Ca}$  from Refs. [49, 59], have been rescaled to match a unique electron energy of 400 MeV.

also show, with the dotted lines, the charge densities and the associated cross sections obtained from phenomenological calculations done by using the Woods-Saxon potential with the parameters given in Ref. [10]. The dashed-dotted lines showing the empirical densities are taken from the compilation of Ref. [46]. The results of our HF calculations show a better agreement with the data than those of the phenomenological calculations.

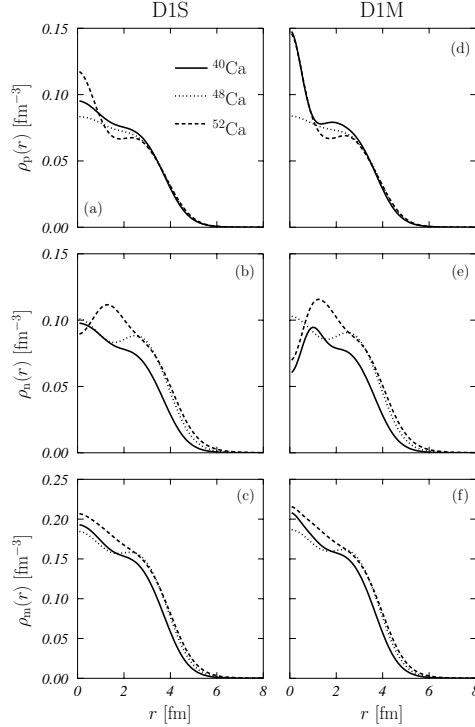


Figure 10: Proton  $\rho_p$ , neutron  $\rho_n$  and matter  $\rho_m$  distributions for the three calcium isotopes, obtained in HF calculations with the D1S and D1M interactions.

The proton, neutron and matter distributions of the three calcium isotopes are shown in Fig. 10. The main features pointed out in the discussion done for the oxygen isotopes are present also in this case, where there are, however,

remarkable differences in the details. In the oxygen isotopes the  $2s_{1/2}$  state was occupied only by the neutrons in the  $^{24}\text{O}$  nucleus. In the calcium isotopes we have considered, the  $2s_{1/2}$  state is always occupied in both proton and neutron cases. The  $^{48}\text{Ca}$  is obtained from the  $^{40}\text{Ca}$  nucleus by filling the neutron  $1f_{7/2}$  state, and the  $^{52}\text{Ca}$  by filling, in addition, the neutron  $2p_{3/2}$  state. In the panel (b) of Fig. 10 it is shown that the filling of the  $1f_{7/2}$  state increases the neutron surface, and leaves practically unmodified the density at the center of the nucleus. The filling of the  $2p_{3/2}$  state modifies the neutron density mainly around 2.0 fm, but it produces also a small lowering at the nuclear center. These modifications change the proton densities at the nuclear center as it is shown in the panel (a). The matter distributions obtained with the D1S interaction, and shown in panel (c), are rather smooth in the nuclear interior. The D1M interaction generates in  $^{40}\text{Ca}$  narrow s-waves, and this produces a large proton distribution in the nuclear center. The corresponding neutron distribution, panel (e), has a hole in the center, and this compensates the peak of the proton distribution and produces a matter distribution rather smooth. The same type of considerations can be done also for the distributions of the  $^{52}\text{Ca}$  isotope. In general, we observe that, as in the oxygen case, the HF calculations find the optimal matter distributions which is rather smooth, even though the separated proton and neutron densities may show some rapid changes.

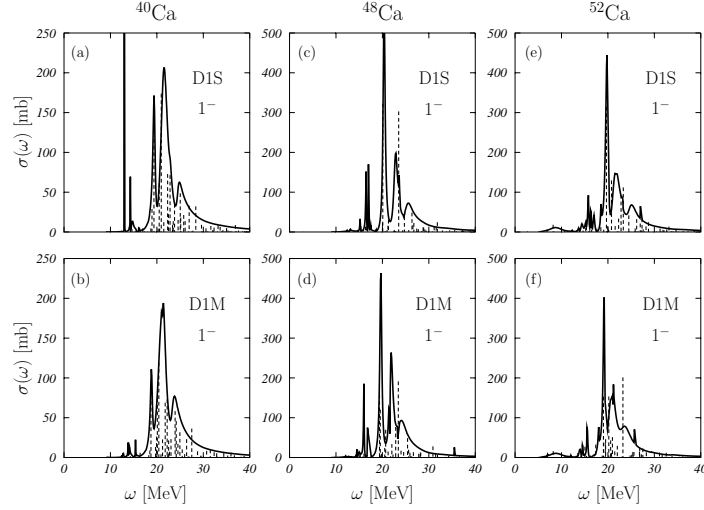


Figure 11: The same as Fig. 4 for the three calcium isotopes. Note that the vertical scale for  $^{40}\text{Ca}$  is half that of  $^{48}\text{Ca}$  and of  $^{52}\text{Ca}$ .

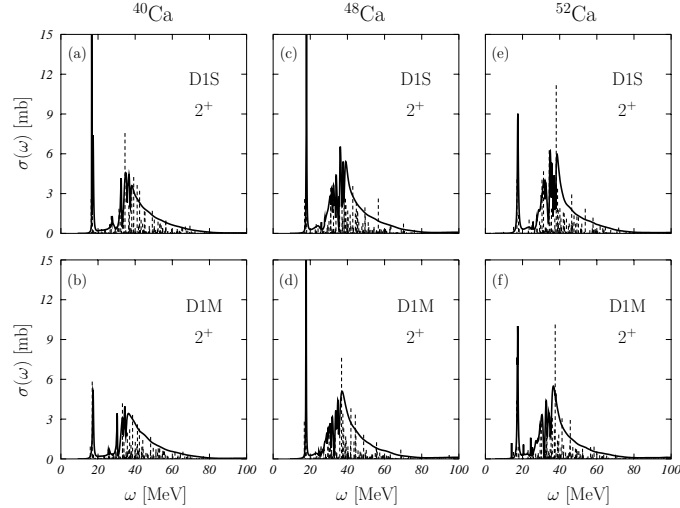


Figure 12: The same as Fig. 5 for the three calcium isotopes.

The comparison between discrete and continuum RPA results is done in Figs. 11 and 12 for the  $1^-$  and  $2^+$  multipole excitations, respectively. As in the oxygen case, we show the contributions to the total photoabsorption cross sections.

The agreement between the results of discrete and continuum RPA calculations is slightly worse than in the oxygen case. Both type of calculations produce resonances, however the total strengths predicted by the discrete RPA are about one half those of the CRPA. For the calcium isotopes, this result is common to all the nuclei, interactions and multipole excitations we have investigated.

	$^{40}\text{Ca}$	$^{48}\text{Ca}$	$^{52}\text{Ca}$
$1^-$			
RPA-D1S	22.37	22.27	20.56
CRPA-D1S	21.89	22.40	20.63
RPA-D1M	22.10	21.86	20.24
CRPA-D1M	22.42	21.77	20.33
$2^+$			
RPA-D1S	24.66	27.34	26.84
CRPA-D1S	25.02	26.89	26.14
RPA-D1M	24.39	26.70	26.12
CRPA-D1M	27.36	26.29	25.49

Table IV: Centroid energies in MeV, Eq. (47), for the  $1^-$  and  $2^+$  electromagnetic excitations in the various calcium isotopes. The discrete RPA results have been obtained by using  $\epsilon_{ph}^{\text{max}}=250$  MeV.

We show in Table IV the centroid energies of the electromagnetic responses obtained in discrete and continuum RPA calculations. As we have done for the oxygen isotopes we have taken for  $\omega_{\text{min}}$  the values corresponding to the continuum thresholds for the various calcium isotopes. The  $1^-$  resonances have been integrated up to  $\omega_{\text{max}}=40$  MeV, while the  $2^+$  resonances up to  $\omega_{\text{max}}=100$  MeV. The relative differences between these centroid energies are smaller than 1% for the  $1^-$  excitations and reach the value of about the 6% for the  $2^+$  states. We have studied separately the centroid energies of the IS and IV components of the  $2^+$  excitations. By selecting the same values of  $\omega_{\text{min}}$  and  $\omega_{\text{max}}$  we reproduce the energy differences of Ref. [30].

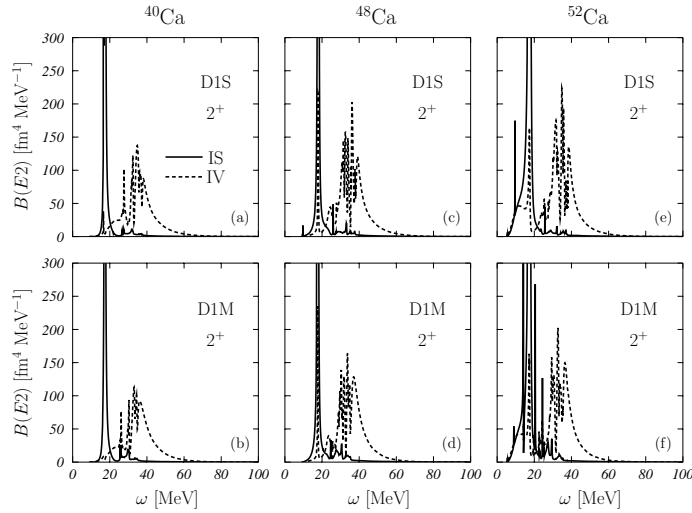


Figure 13: IS and IV strengths of the  $2^+$  excitation mode for the calcium isotopes we have studied.

The structure of the electromagnetic  $2^+$  strength distributions is analogous to that of the oxygen isotopes. They are characterized by a narrow IS peak at lower energies, here around 17-18 MeV, and a much wider IV resonance at higher energies. The IS and IV  $2^+$  responses are separately shown in Fig. 13 for the three calcium isotopes we are studying, and for the two interactions we are using. The peak of the IS  $2^+$  resonance has been identified in  $^{40}\text{Ca}$  at  $17.7 \pm 0.2$  MeV in  $\alpha$  scattering processes [60]. This value should be compared with the peak energy of 17.4 MeV in CRPA calculations done with both D1S and D1M forces. The presence of an IV  $2^+$  resonance in  $^{40}\text{Ca}$  around 32

MeV has been indicated in the analysis of radiative neutron capture data [61]. Our calculations produce wide, and fragmented, IV resonances. We have peaks around 32 MeV but also around 35 MeV.

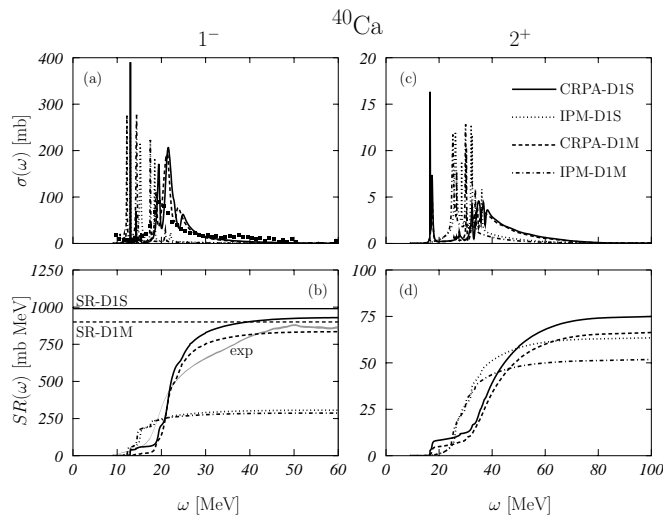


Figure 14: The same as Fig. 7 for  $^{40}\text{Ca}$ . Experimental data (solid squares) are from Ref. [52]. The value of the TRK sum rule is 600 mb MeV.

In Fig. 14 we compare our  $^{40}\text{Ca}$  CRPA results with the total photoabsorption data of Ref. [52] and with the result of the IPM calculations. The same observations done for the oxygen case are valid also here. The IPM results are unable to describe the experimental cross section. The sum rule functions (50) shown in the panels (b) and (d) of the figure confirm what we have observed in the oxygen case. The strengths of the IPM results are much smaller than those of the CRPA calculations. In the  $1^-$  case, the CRPA sum rule function reaches the empirical value but too early with respect to the empirical behaviour. This indicates that the strength is too concentrated in the resonance region.

The value of the traditional TRK sum rule is 600 mb MeV, much lower than the limiting values obtained by our CRPA calculations. The nuclear matter estimates of the enhancement factors gives limiting values of the sum rules of 990 and 900 mb MeV for the D1S and D1M interactions, respectively. We show in the panel (b) of Fig. 14 that these values are compatible with our CRPA results.

Also in the case of the calcium isotopes we have compared our self-consistent CRPA results, with those of the phenomenological approach. We obtain results analogous to those shown in the oxygen case. The phenomenological results show less strength and structure than the self-consistent ones.

## V. CONCLUSIONS

In this article we presented a technique to solve the CRPA equations in a self-consistent framework. In our calculations we used Gogny-like finite-range interactions containing zero-range density dependent terms. Also the spin-orbit term, used only in the HF calculations, is of zero-range type. We have shown results for the  $A = 16, 22$  and  $24$  oxygen isotopes, and for  $A = 40, 48$  and  $52$  calcium isotopes. We have compared our results with the available experimental total photoabsorption data. We have studied the need of a proper treatment of the continuum, by comparing our results with those obtained by discrete RPA calculations. The need of a self-consistent approach has been investigated by making a comparison with the results of phenomenological CRPA calculations.

We summarize here below the main results of our study.

- The D1S and D1M forces are very different if compared in the various interaction channels Eq. (5). However, they produce very similar results, both in HF and in CRPA calculations.
- In the HF calculations the global matter distribution, given by the sum of the proton and neutron distributions, is modified to obtain the minimization of the total energy of the system. We have shown in Figs. 3 and 10 that the HF minimization procedure produces rather smooth matter distributions, even though separately, the proton and neutron densities may strongly variate.

- With the increasing number of neutrons, the protons s.p. states become more bound, as we have shown in Tabs. I and III. This effect is not relevant for the charge conserving excitations, those treated in this work, but it may have consequences in charge exchange excitations.
- The IPM calculations of the nuclear responses are unable to provide the proper strength of the multipole excitation. This confirms a well known fact that IPM calculations do not predict the presence of giant resonances in the nuclear excitation spectrum.
- The comparison with discrete RPA results shows the need of a correct treatment of the continuum in self-consistent calculations. In discrete calculations we have used s.p. configuration spaces large enough to ensure the stability of the results in the low-lying states and in the giant resonance excitation regions. Discrete RPA calculations can reproduce some bulk properties of the excitation, the centroid energies for example, but they fails in the detailed description. Discrete RPA responses show clustering of excited states that the CRPA strength distributions do not have.
- The phenomenological CRPA results are similar to those of the self-consistent CRPA calculations in  $^{16}\text{O}$  and  $^{40}\text{Ca}$ . The input parameters of the phenomenological calculations have been chosen to reproduce some experimental quantities in these nuclei. On the contrary, when we apply this approach to the other isotopes, we found results which are rather different from those obtained with the self-consistent approach. This indicates the inadequacy of the phenomenological approach in the study of nuclei lying in experimentally unexplored parts of the nuclear isotope chart.
- Self-consistent CRPA calculations describe rather well the experimental positions of the giant resonance peaks, for both the  $1^-$  and the  $2^+$  excitations. On the other hand, the strength distributions are incorrect since they are concentrated in the peak region, while the experimental distributions are wider. This is a well known deficiency of the RPA description of nuclear giant resonances. There are strong indications that the problem could be solved by considering the excitation of two particle-two hole pairs [62–64].

The work presented here is the first step of a project aiming to apply a self-consistent computational scheme to many other observables and nuclei. The next step of our work will be the study of unnatural parity excitations, and for this investigation we shall consider a tensor term in the interaction [65]. It has been shown that this term slightly affects the ground state properties, [66, 67] but it has more relevant effects on the spectrum of magnetic states [26, 27]. The study of charge-exchange excitations will be a following step.

### Appendix A: Expansion of the CRPA equations on a basis of sturmian functions

In this appendix we derive Eqs. (39) and (40) by inserting the expansions (37) (38) of the  $f$  and  $g$  functions on the sturmian functions basis in the CRPA secular equations (27) and (28). We insert the expression (37) in the first term of Eq. (27) and, by using the definition (36) of the orthogonalized sturmian functions and the fact that  $R_p(r, \epsilon_p)$  is an eigenfunction of the s.p. hamiltonian  $\mathcal{H}$  (see Eq. (1)) for the eigenvalue  $\epsilon_p = \epsilon_h + \omega$ , we obtain

$$\begin{aligned}
 \mathcal{H}[f_{ph}^{p_0 h_0}(r)] - (\epsilon_h + \omega) f_{ph}^{p_0 h_0}(r) &= \mathcal{H}\left[R_{p_0}(r, \epsilon_p) \delta_{pp_0} \delta_{hh_0} + \sum_{\mu} c_{ph}^{\mu+} \tilde{\Phi}_p^{\mu+}(r)\right] \\
 &\quad - (\epsilon_h + \omega) \left[R_{p_0}(r, \epsilon_p) \delta_{pp_0} \delta_{hh_0} + \sum_{\mu} c_{ph}^{\mu+} \tilde{\Phi}_p^{\mu+}(r)\right] \\
 &= \sum_{\mu} c_{ph}^{\mu+} \left\{ \mathcal{H}[\Phi_p^{\mu+}(r)] - (\epsilon_h + \omega) \Phi_p^{\mu+}(r) \right. \\
 &\quad \left. - \sum_{\epsilon_i < \epsilon_F} \delta_{ip} (\epsilon_i - \epsilon_h - \omega) R_i(r) \int dr' r'^2 R_i(r') \Phi_p^{\mu+}(r') \right\}.
 \end{aligned} \tag{A1}$$

The sum of the last term is limited to the states below the Fermi surface having the same orbital and total angular momentum of the particle state. Using the definition of the Sturm-Bessel functions given in Eq. (33), we obtain for

the above expression

$$\begin{aligned}
\mathcal{H}[f_{ph}^{p_0 h_0}(r)] - (\epsilon_h + \omega) f_{ph}^{p_0 h_0}(r) = \\
= - \sum_{\mu} c_{ph}^{\mu+} \left\{ \left[ \bar{U}_p^{\mu}(r) - \mathcal{U}(r) \right] \Phi_p^{\mu+}(r) + \int dr' r'^2 \mathcal{W}(r, r') \Phi_p^{\mu+}(r') \right. \\
\left. + \sum_{\epsilon_i < \epsilon_F} \delta_{ip} (\epsilon_i - \epsilon_h - \omega) R_i(r) \int dr' r'^2 R_i(r') \Phi_p^{\mu+}(r') \right\}, \tag{A2}
\end{aligned}$$

where we have used the fact that, from Eqs. (1) and (33), we have

$$\mathcal{H}[\Phi_p^{\mu+}(r)] - [\mathcal{U}(r) + \epsilon_p] \Phi_p^{\mu+}(r) + \int dr' r'^2 \mathcal{W}(r, r') \Phi_p^{\mu+}(r') = -\bar{U}_p^{\mu}(r) \Phi_p^{\mu+}(r). \tag{A3}$$

Multiplying the above expression by  $r^2 \Phi_p^{\nu+}(r)$  and integrating on  $r$  we obtain:

$$\begin{aligned}
\int dr r^2 \Phi_p^{\nu+}(r) \left\{ \mathcal{H}[f_{ph}^{p_0 h_0}(r)] - (\epsilon_h + \omega) f_{ph}^{p_0 h_0}(r) \right\} = \\
= - \sum_{\mu} c_{ph}^{\mu+} \left\{ \delta_{\mu\nu} - \int dr r^2 \Phi_p^{\nu+}(r) \left[ \mathcal{U}(r) \Phi_p^{\mu+}(r) - \int dr' r'^2 \mathcal{W}(r, r') \Phi_p^{\mu+}(r') \right. \right. \\
\left. \left. - \sum_{\epsilon_i < \epsilon_F} \delta_{ip} (\epsilon_i - \epsilon_h - \omega) R_i(r) \int dr' r'^2 R_i(r') \Phi_p^{\mu+}(r') \right] \right\} \\
\equiv - \sum_{\mu} c_{ph}^{\mu+} \left\{ \delta_{\mu\nu} - \langle (\Phi_p^{\nu+})^* | \mathcal{U} | \Phi_p^{\mu+} \rangle + \langle (\Phi_p^{\nu+})^* | \mathbb{I} | \mathcal{W} | \Phi_p^{\mu+} \rangle \right. \\
\left. + \sum_{\epsilon_i < \epsilon_F} \delta_{ip} (\epsilon_i - \epsilon_h - \omega) \langle (\Phi_p^{\nu+})^* | R_i \rangle \langle (R_i)^* | \Phi_p^{\mu+} \rangle \right\}, \tag{A4}
\end{aligned}$$

where we have used the orthogonality relation (35). The number of the radial integrations is given by the number of the functions indicated in the bra and ket symbols. For this reason, in the terms with  $\mathcal{W}$  we have inserted  $\mathbb{I}$  to indicate the identity function.

For the right-hand side of Eq. (27), using the orthogonality relation (36) we obtain

$$\begin{aligned}
\int dr r^2 \Phi_p^{\nu+}(r) \left[ -\mathcal{F}_{ph}^J(r) + \sum_{\epsilon_i < \epsilon_F} \delta_{ip} R_i(r) \int dr' r'^2 R_i^*(r') \mathcal{F}_{ph}^J(r') \right] = \\
= - \int dr r^2 \left[ \tilde{\Phi}_p^{\nu+}(r) + \sum_{\epsilon_i < \epsilon_F} \delta_{ip} R_i^*(r) \int dr' r'^2 R_i(r') \Phi_p^{\nu}(r') \right] \mathcal{F}_{ph}^J(r) \\
+ \int dr r^2 \Phi_p^{\nu+}(r) \sum_{\epsilon_i < \epsilon_F} \delta_{ip} R_i(r) \int dr' r'^2 R_i^*(r') \mathcal{F}_{ph}^J(r') \\
= - \int dr r^2 \tilde{\Phi}_p^{\nu+}(r) \mathcal{F}_{ph}^J(r). \tag{A5}
\end{aligned}$$

Using now Eqs. (29), (37) and (38) we have

$$\begin{aligned}
& - \int dr r^2 \tilde{\Phi}_p^{\nu+}(r) \mathcal{F}_{ph}^J(r) = - \int dr r^2 \tilde{\Phi}_p^{\nu+}(r) \sum_{p'h'} \int dr' r'^2 \\
& \quad \left\{ R_{h'}^*(r') \left[ V_{ph,p'h'}^{J,\text{dir}}(r, r') R_h(r) f_{p'h'}^\nu(r') - V_{ph,p'h'}^{J,\text{exc}}(r, r') f_{p'h'}^\nu(r) R_h(r') \right] \right. \\
& \quad \left. + g_{p'h'}^*(r') \left[ U_{ph,p'h'}^{J,\text{dir}}(r, r') R_h(r) R_{h'}(r') - U_{ph,p'h'}^{J,\text{exc}}(r, r') R_{h'}(r) R_h(r') \right] \right\} \\
& = - \int dr r^2 \tilde{\Phi}_p^{\nu+}(r) \sum_{p'h'} \int dr' r'^2 \\
& \quad \left\{ R_{h'}^*(r') V_{ph,p'h'}^{J,\text{dir}}(r, r') R_h(r) \left[ R_{p_0}(r', \epsilon_{p_0}) \delta_{p',p_0} \delta_{h',h_0} + \sum_{\mu} c_{p'h'}^{\mu+} \tilde{\Phi}_{p'}^{\mu+}(r') \right] \right. \\
& \quad - R_{h'}^*(r') V_{ph,p'h'}^{J,\text{exc}}(r, r') \left[ R_{p_0}(r, \epsilon_{p_0}) \delta_{p',p_0} \delta_{h',h_0} + \sum_{\mu} c_{p'h'}^{\mu+} \tilde{\Phi}_{p'}^{\mu+}(r) \right] R_h(r') \\
& \quad + \sum_{\mu} (c_{p'h'}^{\mu-})^* (\tilde{\Phi}_{p'}^{\mu-}(r'))^* \\
& \quad \left. \left[ U_{ph,p'h'}^{J,\text{dir}}(r, r') R_h(r) R_{h'}(r') - U_{ph,p'h'}^{J,\text{exc}}(r, r') R_{h'}(r) R_h(r') \right] \right\} \\
& = - \langle (\tilde{\Phi}_p^{\nu+})^* R_{h_0} | V_{ph,p_0h_0}^{J,\text{dir}} | R_h R_{p_0}(\epsilon_{p_0}) \rangle - \sum_{p'h'} \sum_{\mu} c_{p'h'}^{\mu+} \langle (\tilde{\Phi}_p^{\nu+})^* R_{h'} | V_{ph,p'h'}^{J,\text{dir}} | R_h \tilde{\Phi}_{p'}^{\mu+} \rangle \\
& \quad + \langle (\tilde{\Phi}_p^{\nu+})^* R_{h_0} | V_{ph,p_0h_0}^{J,\text{exc}} | R_{p_0}(\epsilon_{p_0}) R_h \rangle + \sum_{p'h'} \sum_{\mu} c_{p'h'}^{\mu+} \langle (\tilde{\Phi}_p^{\nu+})^* R_{h'} | V_{ph,p'h'}^{J,\text{exc}} | \tilde{\Phi}_{p'}^{\mu+} R_h \rangle \\
& \quad - \sum_{p'h'} \sum_{\mu} (c_{p'h'}^{\mu-})^* \\
& \quad \left[ \langle (\tilde{\Phi}_p^{\nu+})^* \tilde{\Phi}_{p'}^{\mu-} | U_{ph,p'h'}^{J,\text{dir}} | R_h R_{h'} \rangle - \langle (\tilde{\Phi}_p^{\nu+})^* \tilde{\Phi}_{p'}^{\mu-} | U_{ph,p'h'}^{J,\text{exc}} | R_{h'} R_h \rangle \right]. \tag{A6}
\end{aligned}$$

Putting together Eqs. (A4) and (A7), we find a new expression of the CRPA secular equation Eq. (27)

$$\begin{aligned}
& \sum_{\mu} \sum_{p'h'} \left\{ \left[ \delta_{pp'} \delta_{hh'} \left( \delta_{\mu\nu} - \langle (\Phi_p^{\nu+})^* | \mathcal{U} | \Phi_p^{\mu+} \rangle + \langle (\Phi_p^{\nu+})^* | \mathbb{I} | \mathcal{W} | \Phi_p^{\mu+} \rangle \right) \right. \right. \\
& \quad \left. + \sum_{\epsilon_i < \epsilon_F} \delta_{ip} (\epsilon_i - \epsilon_h - \omega) \langle (\Phi_p^{\nu+})^* | R_i \rangle \langle (R_i)^* | \Phi_p^{\mu+} \rangle \right) \\
& \quad - \left( \langle (\tilde{\Phi}_p^{\nu+})^* R_{h'} | V_{ph,p'h'}^{J,\text{dir}} | R_h \tilde{\Phi}_{p'}^{\mu+} \rangle - \langle (\tilde{\Phi}_p^{\nu+})^* R_{h'} | V_{ph,p'h'}^{J,\text{exc}} | \tilde{\Phi}_{p'}^{\mu+} R_h \rangle \right) c_{p'h'}^{\mu+} \\
& \quad \left. - \left( \langle (\tilde{\Phi}_p^{\nu+})^* \tilde{\Phi}_{p'}^{\mu-} | U_{ph,p'h'}^{J,\text{dir}} | R_h R_{h'} \rangle - \langle (\tilde{\Phi}_p^{\nu+})^* \tilde{\Phi}_{p'}^{\mu-} | U_{ph,p'h'}^{J,\text{exc}} | R_{h'} R_h \rangle \right) (c_{p'h'}^{\mu-})^* \right\} = \\
& = \langle (\tilde{\Phi}_p^{\nu+})^* R_{h_0} | V_{ph,p_0h_0}^{J,\text{dir}} | R_h R_{p_0}(\epsilon_{p_0}) \rangle - \langle (\tilde{\Phi}_p^{\nu+})^* R_{h_0} | V_{ph,p_0h_0}^{J,\text{exc}} | R_{p_0}(\epsilon_{p_0}) R_h \rangle. \tag{A7}
\end{aligned}$$

A similar equation can be obtained from Eq. (28) for the  $g$  channel function.

## Appendix B: Continuum wave function with HF potential

We use an expansion on the Sturm-Bessel functions basis to calculate the s.p. wave function for  $\epsilon_p > 0$  with HF mean-field potential. The explicit expression of the differential equation to be solved for the reduced radial part of

the wave function  $u_p(r) = r R_p(r, \epsilon_p)$  is

$$-\frac{\hbar^2}{2m} \left( \frac{d^2}{dr^2} - \frac{l_p(l_p+1)}{r^2} \right) u_p(r) + \mathcal{U}(r) u_p(r) - \int dr' r' \mathcal{W}(r, r') u_p(r') = \epsilon_p u_p(r), \quad (\text{B1})$$

where  $\mathcal{U}$  and  $\mathcal{W}$  have been defined in Eqs. (2) and (3) respectively.

We express the solution of the above equation as

$$\frac{u_p(r)}{r} = j_{l_p}(k_p r) + \sum_{\mu} c_p^{\mu} \Phi_p^{\mu}(r) \quad (\text{B2})$$

where  $j_{l_p}(k_p r)$  is a spherical Bessel function with  $k_p$  the wave number corresponding to  $\epsilon_p$ . Using the definition (33) of the Sturm-Bessel functions, and their orthogonality relation (35), we obtain the following non homogeneous system

$$\begin{aligned} & \sum_{\mu} \left[ \delta_{\mu\nu} - \int dr r^2 \Phi_p^{\nu}(r) \mathcal{U}(r) \Phi_p^{\mu}(r) + \int dr r^2 \Phi_p^{\nu}(r) \int dr' r'^2 \mathcal{W}(r, r') \Phi_p^{\mu}(r') \right] c_p^{\mu} = \\ & = \int dr r^2 \Phi_p^{\nu}(r) \mathcal{U}(r) j_{l_p}(k_p r) - \int dr r^2 \Phi_p^{\nu}(r) \int dr' r'^2 \mathcal{W}(r, r') j_{l_p}(k_p r'), \end{aligned} \quad (\text{B3})$$

where the unknowns are the expansion coefficients  $c_p^{\mu}$ .

### Acknowledgments

We thank I. Sick for providing us with elastic electron scattering data. This work has been partially supported by the Spanish Ministerio de Ciencia e Innovación under contracts FPA2009-14091-C02-02 and ACI2009-1007 and by the Junta de Andalucía (FQM0220).

- 
- [1] R. B. Wiringa, V. G. J. Stoks, R. Schiavilla, Phys. Rev. C 51 (1995) 38.
  - [2] R. Machleidt, Phys. Rev. C 63 (2001) 024001.
  - [3] B. S. Pudliner, V. R. Pandharipande, J. Carlson, S. C. Pieper, R. B. Wiringa, Phys. Rev. C 56 (1997) 1720.
  - [4] S. C. Pieper, K. Varga, R. B. Wiringa, Phys. Rev. C 66 (2002) 044310.
  - [5] S. C. Pieper, R. B. Wiringa, Ann. Rev. Nucl. Part. Sc. 51 (2001) 53.
  - [6] H. Kamada, et al., Phys. Rev. C 64 (2001) 044001.
  - [7] P. Navrátil, J. P. Vary, B. R. Barrett, Phys. Rev. C 62 (2000) 054311.
  - [8] D. J. Dean, M. Hjorth-Jensen, Phys. Rev. C 69 (2004) 054320.
  - [9] S. Gandolfi, F. Pederiva, S. Fantoni, K. E. Schmidt, Phys. Rev. C 73 (2006) 044304.
  - [10] F. Arias de Saavedra, C. Bisconti, G. Co', A. Fabrocini, Phys. Rep. 450 (2007) 1.
  - [11] S. Quaglioni, P. Navrátil, Phys. Rev. C 79 (2009) 044606.
  - [12] R. Roth, T. Neff, H. Feldmeier, Prog. Part. Nucl. Phys. 65 (2010) 50.
  - [13] P. Ring, P. Schuck, The nuclear many-body problem, Springer, Berlin, 1980.
  - [14] J. Speth, E. Werner, W. Wild, Phys. Rep. 33 (1977) 127.
  - [15] J. Speth, V. Klemm, J. Wambach, G. E. Brown, Nucl. Phys. A 343 (1980) 382.
  - [16] A. Migdal, Theory of finite Fermi systems and applications to atomic nuclei, Interscience, London, 1967.
  - [17] G. F. Bertsch, S. F. Tsai, Phys. Rep. 18 (1975) 125.
  - [18] S. Shlomo, G. F. Bertsch, Nucl. Phys. A 243 (1975) 507.
  - [19] K. F. Liu, N. Van Giai, Phys. Lett. B 55 (1976) 23.
  - [20] N. Van Giai, H. Sagawa, Nucl. Phys. A 371 (1981) 1.
  - [21] M. Waroquier, et al., Phys. Rep. 148 (1987) 249.
  - [22] A. M. Saruis, Phys. Rep. 235 (1993) 57.
  - [23] I. Hamamoto, H. Sagawa, X. Z. Zhang, Phys. Rev. C 53 (1996) 765.
  - [24] J. Dechargé, D. Gogny, Phys. Rev. C 21 (1980) 1568.
  - [25] M. Martini, G. Co', M. Anguiano, A. M. Lallena, Phys. Rev. C 75 (2007) 034604.
  - [26] G. Co', A. M. Lallena, Nucl. Phys. A 510 (1990) 139.
  - [27] V. De Donno, G. Co', C. Maieron, M. Anguiano, A. M. Lallena, M. Moreno-Torres, Phys. Rev. C 79 (2009) 044311.
  - [28] T. Udagawa, B. T. Kim, Phys. Rev. C 40 (1989) 2271.
  - [29] M. Buballa, S. Drożdż, S. Krewald, J. Speth, Ann. of Phys. 208 (1991) 346.



- [30] H. Nakada, K. Mizuyama, M. Yamagami, M. Matsuo, Nucl. Phys. A 828 (2009) 283.
- [31] J. Piekarewicz, Phys. Rev. C 64 (2001) 024307.
- [32] O. Bohigas, N. Van Giai, D. Vautherin, Phys. Lett. B 102 (1981) 105.
- [33] A. R. Edmonds, Angular momentum in quantum mechanics, Princeton University Press, Princeton, 1957.
- [34] M. Rotenberg, Ann. Phys. 19 (1962) 262.
- [35] S. Weinberg, Phys. Rev. B. 133 (1963) 232.
- [36] S. Weinberg, Lectures on Particles and Field Theory, Brandeis Summer Institute in Theoretical Physics, S. Deser and K. W. Ford Eds., Prentice-Hall, Englewood Cliffs, 1964.
- [37] G. Newton, Scattering theory of Waves and Particles, McGraw-Hill, New York, 1966.
- [38] G. Rawitscher, Phys. Rev. C. 25 (1982) 2196.
- [39] J. M. Eisenberg, W. Greiner, Excitation Mechanisms of the nucleus, North Holland, Amsterdam, 1970.
- [40] J. M. Blatt, V. F. Weisskopf, Theoretical nuclear physics, John Wiley and sons, New York, 1952.
- [41] J. F. Berger, M. Girod, D. Gogny, Comp. Phys. Commun. 63 (1991) 365.
- [42] S. Goriely, S. Hilaire, M. Girod, S. Péru, Phys. Rev. Lett. 102 (2009) 242501.
- [43] A. Akmal, V. R. Pandharipande, D. G. Ravenhall, Phys. Rev. C 58 (1998) 1804.
- [44] S. Gandolfi, A. Y. Illarionov, S. Fantoni, J. C. Miller, F. Pederiva, K. E. Schmidt, Mont. Not. R. Astron. Soc. 404 (2010) L35.
- [45] G. Co', V. De Donno, C. Maieron, M. Anguiano, A. M. Lallena, Phys. Rev. C 80 (2009) 014308.
- [46] C. W. De Jager, C. De Vries, At. Data Nucl. Data Tables 36 (1987) 495.
- [47] R. Anni, G. Co', P. Pellegrino, Nucl. Phys. A 584 (1995) 35.
- [48] I. Sick, J. McCarthy, Nucl. Phys. A 150 (1970) 631.
- [49] I. Sick, private communication.
- [50] J. Daoutidis, P. Ring, Phys. Rev. C 80 (2009) 024309.
- [51] K. T. Knöpfle, G. J. Wagner, H. Breuer, M. Rogge, C. Mayer-Böricke, Phys. Rev. Lett. 35 (1975) 779.
- [52] J. Ahrens, et al., Nucl. Phys. A 251 (1975) 479.
- [53] M. Traini, G. Orlandini, R. Leonardi, Rivista Nuovo Cimento 10 (1987) 1.
- [54] R. de Haro, S. Krewald, J. Speth, Nucl. Phys. A 388 (1982) 265.
- [55] G. Co', S. Krewald, Nucl. Phys. A 433 (1985) 392.
- [56] B. B. P. Sinha, G. Peterson, R. R. Whitney, I. Sick, J. McCarthy, Phys. Rev. C 7 (1973) 1930.
- [57] I. Sick, J. Bellicard, J. Cavedon, B. Frois, M. Huet, P. Leconte, P. Ho, S. Platchkov, Phys. Lett. B 88 (1979) 240.
- [58] J. M. Cavedon, Ph.D. thesis, Université de Paris-Sud (France), unpublished (1980).
- [59] I. Sick, Model-independent densities of s/d-shell nuclei, unpublished (1975).
- [60] Y.-W. Lui, J. D. Bronson, C. M. Rozsa, D. H. Youngblood, P. Bogucki, U. Garg, Phys. Rev. C 24 (1981) 884.
- [61] I. Bergqvist, R. Zorro, A. Håkansson, A. Lindholm, L. Nilsson, N. Olsson, A. Likar, Nucl. Phys. A 419 (1984) 509.
- [62] S. Drożdż, S. Nishizaki, J. Speth, J. Wambach, Phys. Rep. 197 (1990) 1.
- [63] S. Kamerdzhiev, J. Speth, G. Tertychny, Phys. Rep. 393 (2004) 1.
- [64] D. Gambacurta, M. Grasso, F. Catara, Phys. Rev. C 81 (2010) 054312.
- [65] G. Co', V. De Donno, M. Anguiano, A. M. Lallena, arXiv:1009.3364 [nucl-th].
- [66] T. Otsuka, T. Matsuo, D. Abe, Phys. Rev. Lett. 97 (2006) 162501.
- [67] M. Moreno-Torres, M. Grasso, H. Liang, V. de Donno, M. Anguiano, N. Van Giai, Phys. Rev. C 81 (2010) 064327.